Optimal Growth in Inertia-Gravity Wave Packets: Energetics, long-term development, and three-dimensional structure

Ulrich Achatz and Gerhard Schmitz

Leibniz-Institut für Atmosphärenphysik an der Universität Rostock

Kühlungsborn, Germany

submitted to *J. Atmos. Sci.* April 6th 2004

revised March 1st 2005

Ulrich Achatz
Leibniz-Institut für Atmosphärenphysik an der Universität Rostock
Schlossstr. 6
18225 Kühlungsborn
Germany
Tel.: +49-38293-68340
Fax: +49-38293-6850
e-mail: achatz@iap-kborn.de

Abstract

Using a hierarchy of three models of increasing realism and complexity, and expanding on a previous study, optimal perturbations to inertia-gravity wave (IGW) packets are studied with respect to several aspects. It is shown that normal modes are comparatively less able to extract energy from the IGW over finite time due to their time-invariant structure, while singular vectors (SV) can adjust their dynamical fields flexibly so as to optimize the statically enhanced roll and Orr mechanisms by which they grow. On longer time scales, where the time dependence of the IGW packet precludes a normal-mode analysis, optimal growth is found to further amplify suitable perturbations. The propagation characteristics of these exhibit critical-layer interactions for horizontal propagation directions transverse with respect to the IGW, preventing significant vertical propagation, while parallel and obliquely propagating perturbations of sufficiently long horizontal scales are found to radiate gravity waves into altitudes not directly affected by the IGW. SV with shorter wavelengths, as found for short optimization times, stay confined via a linear wave duct near the altitude of least static stability where they are excited. At optimization times of the order of the IGW period the leading SV, with an energy growth by about three orders of magnitude, propagate obliquely, possibly in correspondence to previous results by others from simulations of nonlinear IGW breakdown. The three-dimensional structure of SV shows an amplitude modulation strictly confining the perturbations also to the horizontal location of least static stability, suggesting a picture of turbulence onset in IGW packets where local patches of growing perturbations dominate initially.

1 Introduction

In an examination of the possibility of rapid transient growth of perturbations to an upwardly propagating inertia-gravity wave (IGW) packet in the mesosphere we have recently identified corresponding optimal perturbations (Achatz and Schmitz, 2005, henceforth called AS). These are to be distinguished from the normal modes (NM) calculated by Fritts and Yuan (1989), Yuan and Fritts (1989), Dunkerton (1997), and Kwasniok and Schmitz (2003). While in the parameter range examined we have found, in basic agreement with similar results by Yau et al. (2004), normal modes to grow at most only very weakly at wave amplitudes below the static instability limit, optimal perturbations and the hence developing singular vectors (SV) are seen to still exhibit an energy gain by nearly a factor 100 within one Brunt-Vaisala period. Therefore optimal perturbations might be more appropriate for describing the incipient turbulence onset in a subcritical IGW. At least in part, frequent rocket measurements of considerable turbulent dissipation rates in a statically stable environment (Lübken, 1997) could eventually also be attributed to the hence ensuing wave breaking.

With the intention to deepen our understanding of subcritical IGW instability we expand in this study on the results of AS. First, due to space restrictions the mechanism by which the identified patterns extract their energy from the basic IGW packet had been given only limited attention. It seems worthwhile to look explicitly at the relevant energy exchange terms in their time development and examine what they can teach us about the process. This can also be seen as a good preparation for the second issue treated here. Since AS has its focus on rapid transient development over very short time scales of the order of the Brunt-Vaisala period, an obvious open question is that about the long-

term development of the optimal perturbations found there, as well as how they change as the optimization time is varied over which their energy growth is optimal. Finally the previous work has been restricted to the analysis of vertical profiles of flow field and buoyancy obtained from an IGW packet at the horizontal location where, based on total Brunt-Vaisala frequency and local Richardson number, it might be assumed to be least stable. In this approximation the horizontal structure of the optimal perturbations is that of a plane monochromatic wave propagating at some azimuth angle α with respect to the basic IGW. Driven by the transverse-wind shear in the basic wave via a statically amplified roll mechanism, relate to the one discussed by Farrell and Ioannou (1993a,b) and Bakas et al. (2001), we found, for slightly subcritical IGW with intermediate ratios $R = f/\omega$ between local coriolis parameter and wave frequency, parallel perturbations ($\alpha = 0°$) to amplify most vigorously over one Brunt-Vaisala period. Their scales are rather short (a few 100 m for an IGW with 6 km vertical wavelength), while transverse optimal perturbations ($\alpha = 90°$), to some part subject to energy input from the IGW via a statically amplified Orr mechanism, are longer in scale (a few km). An obvious question we want to address here is what remains of these patterns as one analyzes the fully two-dimensional and time-dependent IGW packet.

We have organized the paper as follows: Section 2 describes our model hierarchy and introduces the problem in general. In section 3 we discuss the energetics of SV in the stratified-shear layer approximation of the IGW, while in section 4 the results are generalized to the analysis of SV for a time dependent vertical profile of IGW at the horizontal location of least initial static stability, allowing also the treatment of long optimization times. Section 5 further moves to the analysis of an IGW packet with its

full horizontal dependence, and section 6 summarizes and discusses the results.

2 Singular vectors for an IGW in a Boussinesq fluid

Only a very short sketch is given here of our model environment and the concept of singular vectors within it. For details readers are referred to AS and the literature cited there.

2.1 Model and IGW packet

The equations we are using are the three-dimensional viscous Boussinesq equations with thermal diffusivity on an f plane. The model variables comprise the three-dimensional velocity field $\widehat{\mathbf{v}} = (\widehat{u}, \widehat{v}, \widehat{w})$ and buoyancy $\widehat{b} = g(\widehat{\theta} - \overline{\theta}(z))/\theta_0$. Here $\widehat{\theta}$ denotes potential temperature, $\overline{\theta}(z)$ a merely vertically dependent reference profile, and θ_0 a constant characteristic value. The reference potential temperature also defines the squared background Brunt-Vaisala frequency $N^2 = (g/\theta_0)d\overline{\theta}/dz$, where g is the vertical gravitational acceleration. For viscosity ν and thermal diffusivity μ we use the typical mesospheric values $\nu = \mu = 1\mathrm{m}^2/\mathrm{s}$. The f plane is located at 45° N latitude. $N = 10^{-2}\mathrm{s}^{-1}$ is our Brunt-Vaisala frequency[1]. The model equations have been discretized using second-order finite central differences on a staggered C grid (Tapp and White, 1976). The boundary conditions are triply periodic. It was always made sure that the boundaries are far enough from the instability in order not to affect our results. Monochromatic gravity waves are an exact solution of the nonlinear Boussinesq equations. Among these, waves

[1]This is a rather low value for the mesosphere which has, however, also been used by others (e.g. Fritts et al., 2003). Our results are not much affected by this choice (Achatz and Schmitz, 2005).

with a nearly vertical wavenumber vector are strongly influenced by the Coriolis effect, leading to a near-inertial period, an elliptic polarization of the horizontal velocity field, and a negligible component in the vertical wind. From the structure of such an upwardly propagating wave with typical observed wavelengths (in x direction $\Lambda_x = 500$ km, and in the vertical $\Lambda_z = 3$ km, 6 km, or 9 km) an initial wave packet has been formed by means of a gaussian envelope with half-width Λ_z which then has been integrated in the nonlinear Boussinesq equations. The initial wave phase was chosen so that $x = \Lambda_x/2$ is the horizontal location where the initial vertical wave profile exhibits least static stability. Vertically, the wave packet maximum and location of least static stability is initially right at the center of the model, i.e. at $z = 0$. The resulting time-dependent wave packet is denoted by $\left(\widehat{\mathbf{v}}, \widehat{b}\right) = (\mathbf{V}_0, B_0)(x, z, t)$.

Now let $\left(\widehat{\mathbf{v}}, \widehat{b}\right)(\mathbf{x}, t) = (\mathbf{V}_0, B_0)(x, z, t) + (\mathbf{v}', b')(\mathbf{x}, t)$ be a decomposition of an arbitrary model trajectory into IGW packet and perturbation. We study the dynamics of the perturbation by linearizing the equations about the IGW packet. The latter is symmetric in y so that we can use the ansatz $(\mathbf{v}', b', p') = (\mathbf{v}, b, p)(x, z)\exp(ily)$ with an arbitrary wavenumber l, while p' denotes pressure. This yields

$$\nabla_2 \cdot \mathbf{v} = 0 \tag{1}$$

$$\frac{D\mathbf{v}}{Dt} + u\frac{\partial \mathbf{V}_0}{\partial x} + w\frac{\partial \mathbf{V}_0}{\partial z} + f\mathbf{e}_z \times \mathbf{v} + \nabla_2 p - \mathbf{e}_z b = \nu\nabla_2^2 \mathbf{v} \tag{2}$$

$$\frac{Db}{Dt} + u\frac{\partial B_0}{\partial x} + N_{tot}^2 w = \mu\nabla_2^2 b \quad , \tag{3}$$

where $\mathbf{e}_z$ is the vertical unit vector, $\nabla_2 = (\partial/\partial x, il, \partial/\partial z)$, $D/Dt = \partial/\partial t + \mathbf{V}_0 \cdot \nabla_2$, and $N_{tot}^2 = N^2 + \partial B_0/\partial z$.

In AS we used two simplifications of these equations. In the first we assumed the IGW field to be horizontally symmetric, with the same values as the vertical profile at

$x = \Lambda_x/2$, i.e. at the statically least stable horizontal location at $t = 0$, and further assumed $W_0 = 0$. We further neglected the time dependence of the IGW, which will not be done here. For the horizontally symmetric profile one can use the ansatz $(\mathbf{v}', b', p') = (\mathbf{v}, b, p)(x, z)\exp[i(kx + ly)]$. Usually we express the horizontal wavenumber vector of the perturbation as $(k, l) = k_\parallel(\cos\alpha, \sin\alpha)$ in terms of parallel wavenumber $k_\parallel$ and azimuth angle α. For the analysis it is further useful to use rotated horizontal coordinates $\left(x_\parallel, y_\perp\right)$ pointing in the direction of the horizontal perturbation wave vector and perpendicular to it. The corresponding velocity components being $\left(u_\parallel, v_\perp\right)$ for the perturbation and $\left(U_\parallel, V_\perp\right)$ for the IGW one can also introduce streamfunction ψ and related vorticity $\zeta = (k_\parallel^2 - \partial^2/\partial z^2)\psi$ so that $(u_\parallel, w) = (-\partial/\partial z, ik_\parallel)\psi$.

In the final level of simplification we assumed the vertical profile to be given by the tangents at the statically least stable altitude, i.e. $(U_0, V_0, N_{tot}^2) = [u_0, \beta z, N^2(1 - a)]$ with $u_0 = a\Omega_-/K$ and $\beta = afM/K$, where a is the IGW amplitude at $z = 0$ with respect to static instability, $(K, M) = (2\pi/\Lambda_x, 2\pi/\Lambda_z)$ its two-dimensional wave vector, and $\Omega_- = -\left(N^2K^2 + f^2M^2\right)^{1/2}/\left(K^2 + M^2\right)^{1/2}$ its frequency. In this stratified constant-shear layer we then set $(\psi, \zeta, v_\perp, b)(z, t) = \int_{-\infty}^{\infty} dm\,(\psi_m, \zeta_m, v_m, b_m)(t)\exp\left[i\left(m_t z - k_\parallel u_c t\right) - D\right]$ with $\beta_{s,c} = \beta(\sin\alpha, \cos\alpha)$ and $u_c = u_o\cos\alpha$, $m_t = m - k_\parallel\beta_s t$ a time dependent vertical wavenumber, and $D = \nu\int_0^t d\tau K_t^2(\tau)$ the viscous-diffusive damping increment (assuming $\mu = \nu$), while $K_t^2 = k_\parallel^2 + m_t^2$, and $\zeta_m = K_t^2\psi_m$, thus obtaining decoupled equations for each combination of ψ_m, v_m, and b_m. For $N_{tot}^2 = N^2$ optimal growth in a corresponding stratified shear layer has been studied by Farrell and Ioannou (1993a) and Bakas et al. (2001), whose results are here used and expanded upon.

2.2 Singular vectors

Following Farrell (1988a,b) the leading optimal perturbation $(\mathbf{v}', b')(\mathbf{x}, t = 0)$ to the time dependent IGW packet is that among all possible ones maximizing within the linear model the relative energy growth $E(\tau)/E(0)$ between initialization and some predefined time τ, where $E = 1/2 \oint_V dV(|\mathbf{v}'|^2 + b'^2/N^2)$. The time-dependent singular vectors resulting from the initial optimal perturbations are to be distinguished from the better known normal modes which have a time dependence $\propto \exp[-i(\omega + i\gamma)t]$ with eigenfrequency ω and growth rate γ. Leading normal mode and leading singular vector only coincide for a time-independent background, and as $t \to \infty$. Provided transient growth considerably more rapid than that of normal modes can be identified by the analysis the corresponding structures seem better qualified for a description of the initial instability of an IGW packet. One observes that normal modes always have the same oscillating structure which is simply growing or decaying in time. This is not the case for singular vectors. Their structure can differ quite a lot between initialization and subsequent time. As a consequence, the exchange processes between perturbation and background responsible for the change in amplitude are always the same for a normal mode, while they can vary considerably in the development of a singular vector. This leads to a higher efficiency in the finite-time energy exchange between perturbation and IGW packet, so that optimal perturbations often can grow much more rapidly than normal modes.

3 Energetics and temporal development in the stratified-shear-layer approximation

For each combination of k and l, i.e. $k_\parallel$ and α, and m in the stratified shear layer energy is given by $E_{klm} = \left(K_t^2 \left|\psi_m\right|^2 + \left|v_m\right|^2 + \left|b_m\right|^2 / N^2\right) \exp\left(-2D\right)/2$, for which one can derive from the model equations given in AS

$$\frac{dE_{klm}}{dt} = r_\parallel + r_\perp + r_b + r_d \tag{4}$$

$$r_\parallel = m_t k_\parallel \beta_s \left|\psi_m\right|^2 e^{-2D} \tag{5}$$

$$r_\perp = -k_\parallel \beta_c \Im\left(v_m \overline{\psi}_m\right) e^{-2D} \tag{6}$$

$$r_b = k_\parallel \left(1 - \frac{N_{tot}^2}{N^2}\right) \Im\left(b_m \overline{\psi}_m\right) e^{-2D} \tag{7}$$

$$r_d = -2\nu K_t^2 E_{klm} \quad , \tag{8}$$

containing successively the Reynolds exchange terms due to the fluxes of momentum in $x_\parallel$- and $y_\perp$-direction and of buoyancy against the respective gradients in the shear layer, and viscous-diffusive damping. Defining an instantaneous growth rate $\Gamma = (1/2E_{klm})\,(dE_{klm}/dt)$ one obtains the respective components $\Gamma_\parallel, \Gamma_\perp, \Gamma_b$, and Γ_d. On the basis of these terms the time development of the leading optimal perturbations is analyzed, focussing on the two cases of parallel ($\alpha = 0°$) and transverse ($\alpha = 90°$) propagation where simple closed analytic solutions of the initial-value problem exist.

3.1 Parallel singular vectors

In the limit $\beta^2/\left|N_{tot}\right|^2 = 1/\left|\mathrm{Ri}\right| \gg 1 \gg \left|N_{tot}\right|^2/N^2$ it is shown in AS that the leading parallel singular vector is for some complex a_v

$$\psi_m = \frac{a_v}{2K_0}\frac{|N_{tot}|}{|\beta|}\frac{N_{tot}}{|N_{tot}|}\frac{\beta}{|\beta|}\left(e^{i\phi}-e^{-i\phi}\right) \tag{9}$$

$$b_m = -\frac{a_v}{2}N\frac{|N_{tot}|}{|\beta|}\frac{N_{tot}}{N}\frac{N_{tot}}{|N_{tot}|}\frac{\beta}{|\beta|}\left(e^{i\phi}+e^{-i\phi}\right) \tag{10}$$

$$v_m = -\frac{a_v}{2}\left(e^{i\phi}+e^{-i\phi}\right)+a_v \quad , \tag{11}$$

where $K_0^2 = k_\parallel^2 + m^2$, and $\phi = \widehat{\Omega}t$ with $\widehat{\Omega} = N_{tot}k_\parallel/K_0$. From $\beta_s = 0$ follows $r_\parallel = 0$. From (9)–(11) one derives for $a < 1$ under consistent assumptions

$$E_{klm} = \frac{\left|a_v\right|^2}{2}e^{-2D}\left[4\sin^4\left(\frac{\widehat{\Omega}}{2}t\right)+\left|\mathrm{Ri}\right|\frac{\left|N_{tot}\right|^2}{N^2}\right] \tag{12}$$

$$r_\perp = 2\frac{k_\parallel}{K_0}\left|N_{tot}\right|\left|a_v\right|^2 e^{-2D}\sin\left(\widehat{\Omega}t\right)\sin^2\left(\frac{\widehat{\Omega}}{2}t\right) \tag{13}$$

$$r_b = \left|\mathrm{Ri}\right|\frac{k_\parallel}{K_0}\left|N_{tot}\right|\left(1-\frac{N_{tot}^2}{N^2}\right)\frac{\left|a_v\right|^2}{2}e^{-2D}\sin\left(2\widehat{\Omega}t\right) \quad , \tag{14}$$

where in (12) the small term $\left|\mathrm{Ri}\right|\left|N_{tot}\right|^2/N^2$ has been kept for consistency with the calculated growth factor, while in (14) N_{tot}^2/N^2 has not been neglected in comparison with 1 in order to ensure that $r_b = 0$ for $N_{tot}^2 = N^2$. For $a < 1$ one thus sees the energy of the singular vectors to perform a damped oscillation with period $T = 2\pi/\widehat{\Omega}$. Note that for the perturbation growing at fixed m most strongly over the optimization time τ one has for $\tau > 2\pi/N_{tot}$ the identity $\widehat{\Omega}\tau = \pi$ (see AS) and hence $T = 2\tau$. Similar oscillatory behavior is exhibited by the exchange terms. Generally $r_\perp$ is the larger term besides near $t = nT$ for some integer n, where both vanish but $r_\perp$ has zero time derivative and thus the increase in r_b is steeper.

The corresponding relations for $a > 1$ are obtained by the replacements $\sin \to \sinh$ and $\widehat{\Omega} \to \left|\widehat{\Omega}\right|$. Then no oscillation results but a convergence of the total growth rate

towards that of the corresponding normal mode, i.e. $\Gamma \to \left|N_{tot}k_\parallel/K_0\right|$, which is due to the convergence of the optimal perturbation towards the structure of the normal mode. It is interesting to observe that as a result of the strong normal-mode component in $v_\perp$, induced by the shear gradient, $\Gamma_b/\Gamma_\perp = r_b/r_\perp \to |\mathrm{Ri}|\,(1 - N_{tot}^2/N^2) \ll 1$ although the total growth rate of the normal mode is not influenced by the shear. The exact growth-rate decomposition, obtained from an integration of the exact optimal perturbations (i.e. at optimal $k_\parallel$) at $\lambda_z = 2\pi/m = 0.1\Lambda_z = 600$ m and four representative combinations of a and τ, is shown in figure 1. Note that in the case $(a, \tau) = (0.9, 10\mathrm{min})$ the optimal value of $k_\parallel \approx 2\pi/380\mathrm{m}$ yields $T \approx 3.9\tau$, which is in quite good agreement with the observed exact behavior.

3.2 Transverse singular vectors

As discussed in AS the time-dependent leading transverse singular vector is a two-dimensional structure in the velocity field. On has $v_m = 0$, and in a WKB approximation in the limit $|N_{tot}|^2/N^2 \ll 1$ for some complex a_+

$$\psi_m = -a_+ \frac{g^{3/4}}{K_0}\left(e^{i\phi} - e^{-i\phi}\right) \tag{15}$$

$$b_m = a_+ N_{tot} g^{1/4}\left(e^{i\phi} + e^{-i\phi}\right) \tag{16}$$

with $g = K_0^2/K_t^2$ and $\phi(t) = \int_0^t dt' N_{tot}k_\parallel/K_t(t')$. One obtains generally $r_\perp = 0$ (since $\beta_c = 0$), and for $a < 1$

$$E_{klm} = 2g^{1/2}\,|a_+|^2\, e^{-2D}\left(\sin^2\phi + \frac{|N_{tot}|^2}{N^2}\cos^2\phi\right) \tag{17}$$

$$r_\parallel = 4g^{3/2}\frac{k_\parallel m_t}{K_0^2}\beta\,|a_+|^2\, e^{-2D}\sin^2\phi \tag{18}$$

$$r_b = 2g\frac{k_\parallel}{K_0}\,|N_{tot}|\left(1 - \frac{N_{tot}^2}{N^2}\right)|a_+|^2\, e^{-2D}\sin 2\phi \quad . \tag{19}$$

The corresponding relations for $a > 1$ result from the replacements $(\cos, \sin) \rightarrow (\cosh, \sinh)$ and $\phi \rightarrow |\phi|$. One sees that for $|\mathrm{Ri}| \ll 1$ growth and decay are generally dominated by $r_{\parallel}$. As also discussed in AS, at fixed initial vertical wavenumber m largest growth over τ is obtained at $k_{\parallel} = m/\beta\tau$, implying $m_t = m\,(1 - t/\tau)$ so that decay sets in at $t = \tau$. Only near $t = 0$, when both $r_{\parallel}$ and r_b approximately vanish, the latter dominates since the former there has zero time derivative. The large-time asymptotic behavior, incorrectly predicted by the WKB approximation, is best determined directly from the model equations (see AS) whence one finds, similarly to Farrell and Ioannou (1993a), that $(\psi_m, b_m) \propto t^{\sqrt{1/4 - N_{tot}^2/\beta^2} - 1/2}\,(t^{-1}, 1)$ for $t \rightarrow \infty$ so that $E_{klm} \propto t^{\sqrt{1 - 4N_{tot}^2/\beta^2} - 1} \exp(-2D)$. Thus even in the absence of viscosity and diffusion energy eventually decays for $a < 1$, while for $a > 1$ a final decay is caused by viscous-diffusive damping. For the same four cases as used before the exact time-dependent growth-rate decomposition of the optimally growing perturbation (i.e. with optimal $k_{\parallel}$) is shown in figure 2. One sees that the relative importance of Γ_b decreases with increasing τ, which can be understood by noting that, up to the phase factors, at the optimal wavenumber $r_b/r_{\parallel} \propto \left(\sqrt{|\mathrm{Ri}|}/2\right)\left[1/\beta^2\tau^2 + (1 - t/\tau)^2\right]^{1/2} / (1 - t/\tau)$ so that near $t = 0$ the ratio decreases with increasing τ.

3.3 Dependence on azimuth angle

For general azimuth angles the behavior is a transition between the two cases discussed above. In figure 3 we show for the same four combinations of a and τ as above the exact time dependence of energy for four representative azimuth angles. One observes for $\alpha = 0$ the damped oscillation at $a < 1$, and the exponential divergence at $a > 1$ which only is obstructed by viscous-diffusive damping if $D > \left|\widehat{\Omega}\right|$. For larger azimuth angles one sees at

$t = \tau$ the peak or sudden reduction of further growth as predicted by WKB theory. The general large-time asymptotic behavior is similar to the transverse case, i.e. $(\psi_m, b_m) \propto t^{\sqrt{1/4-N_{tot}^2/\beta_s^2}-1/2}\,(t^{-1}, 1)$ and $v_m \to v_m(t=0) - \beta_c/N_{tot}^2 b_m(t=0) + o\left(t^{\sqrt{1/4-N_{tot}^2/\beta_s^2}-1/2}\right)$ for $t \to \infty$ so that the energy in ψ_m and b_m is $\propto t^{\sqrt{1-4N_{tot}^2/\beta_s^2}-1}\exp(-2D)$ while that in v_m asymptotes towards a constant in the inviscid-nondiffusive limit (following from the conservation of $v_m/\beta_c - b_m/N_{tot}^2$, see also Bakas et al., 2001). In the general case viscous and diffusive damping eventually prevails since $D \propto t^3$ for large times, but a transition phase of algebraic growth at $a > 1$ for $t > \tau$ is visible for the two intermediate azimuth angles.

4 Energetics and temporal development in the time dependent 1D profile

In the approximation of the IGW packet following the constant-shear layer picture in complexity it is approximated by its vertical profile at $x = \Lambda_x/2$. In contrast to AS we also consider the long-term development of the SV, so that the time-dependence of this profile is not neglected. Also here the SV dynamics is studied using energy considerations. From the model equations in AS one finds

$$\frac{\partial}{\partial t}\frac{\left|u_\parallel\right|^2}{2} + \Re\left(p\frac{\partial \overline{w}}{\partial z}\right) - \nu\frac{\partial^2}{\partial z^2}\frac{\left|u_\parallel\right|^2}{2} - f\Re\left(u_\parallel \overline{v}_\perp\right) = r_\parallel - \nu\left(k_\parallel^2\left|u_\parallel\right|^2 + \left|\frac{\partial u_\parallel}{\partial z}\right|^2\right) \quad (20)$$

$$\frac{\partial}{\partial t}\frac{|v_\perp|^2}{2} - \nu\frac{\partial^2}{\partial z^2}\frac{|v_\perp|^2}{2} + f\Re\left(u_\parallel \overline{v}_\perp\right) = r_\perp - \nu\left(k_\parallel^2|v_\perp|^2 + \left|\frac{\partial v_\perp}{\partial z}\right|^2\right) \quad (21)$$

$$\frac{\partial}{\partial t}\frac{|w|^2}{2} + \Re\left(\overline{w}\frac{\partial p}{\partial z}\right) - \nu\frac{\partial^2}{\partial z^2}\frac{|w|^2}{2} = e_{bw} - \nu\left(k_\parallel^2|w|^2 + \left|\frac{\partial w}{\partial z}\right|^2\right) \quad (22)$$

$$\frac{\partial}{\partial t}\frac{|b|^2}{2N^2} - \mu\frac{\partial^2}{\partial z^2}\frac{|b|^2}{2N^2} = r_b - e_{bw} - \frac{\mu}{N^2}\left(k_\parallel^2|b|^2 + \left|\frac{\partial b}{\partial z}\right|^2\right) \quad (23)$$

yielding for the energy density $e_{kl} = 1/2\left(|\mathbf{v}|^2 + |b|^2/N^2\right)$

$$\frac{\partial e_{kl}}{\partial t} + \frac{\partial}{\partial z}\left[\Re\left(\overline{w}p\right) - \nu\frac{\partial}{\partial z}\frac{|\mathbf{v}|^2}{2} - \mu\frac{\partial}{\partial z}\frac{|b|^2}{2N^2}\right] = r_{\parallel} + r_{\perp} + r_b - D_v - D_b \tag{24}$$

with

$$\begin{aligned}
r_{\parallel} &= -\Re\left(u_{\parallel}\overline{w}\right)\frac{\partial U_{\parallel}}{\partial z} && (25)\\
r_{\perp} &= -\Re\left(v_{\perp}\overline{w}\right)\frac{\partial V_{\perp}}{\partial z} && (26)\\
r_b &= -\Re\left(b\overline{w}\right)\frac{1}{N^2}\frac{\partial B_0}{\partial z} && (27)\\
e_{bw} &= \Re\left(b\overline{w}\right) && (28)\\
D_v &= \nu\left[k_{\parallel}^2|\mathbf{v}|^2 + \left|\frac{\partial \mathbf{v}}{\partial z}\right|^2\right] && (29)\\
D_b &= \frac{\mu}{N^2}\left[k_{\parallel}^2|b|^2 + \left|\frac{\partial b}{\partial z}\right|^2\right] \quad . && (30)
\end{aligned}$$

Integrating (24) in the vertical one sees that total energy $E_{kl} = \oint_{L_z} dz e_{kl}$ is subject to changes by the flux of momentum in $x_{\parallel}$- and $y_{\perp}$-direction against the corresponding gradients in the IGW ($r_{\parallel}$ and $r_{\perp}$), the counter-gradient flux of buoyancy (r_b), and viscous and diffusive damping (D_v and D_b). In the same manner as above we calculate from these terms and energy an instantaneous growth rate $\Gamma = 1/\left(2E_{kl}\right) dE_{kl}/dt$ and its decomposition.

4.1 Short optimization times

For the analysis of the dynamics of optimal perturbations at short optimization times we look at $\tau = 10$ min and focus on the two exemplary cases $\alpha = 0°$ and $\alpha = 90°$. Intermediate azimuth angles can be seen as a transition between theses two cases.

4.1.1 Parallel SV

In the left column of figure 4 we show for the leading parallel optimal perturbation (i.e. at optimal horizontal wavelength) energy for $a = 0.9$ and 1.1, and the growth-rate decomposition for $a = 0.9$ from integrations over four optimization periods. Because in the supercritical case $a = 1.1$ at the horizontal wavelength of the leading SV also an unstable normal mode exists (cf. AS) one sees the energy to eventually diverge exponentially, indicating that the structure of the SV has approached that of the normal mode. Figure 5 gives a comparison between the altitude dependent contributions to the total growth rate at $t = 0$ and $t = \tau$ for leading parallel optimal perturbation and normal mode (at the same horizontal wavelength) at $a = 1.1$, i.e. e.g. $\gamma_{\parallel} = r_{\parallel} / \langle 2e_{kl} \rangle$ for the flux of parallel momentum so that $\Gamma_{\parallel} = \left\langle \gamma_{\parallel} \right\rangle$ and likewise for all other terms (angle brackets indicate a vertical average multiplied by L_z/Λ_z). Two aspects are notable there. First, the normal mode does not exhibit any time dependence in its growth-rate decomposition. This is due to its time-independent structure which in turn precludes a dynamic development as seen in the SV which can thereby extract energy from the basic wave in a much more efficient manner. Secondly, in the later stages the exchange processes do not differ any more between singular vector and normal mode, so that obviously the singular vector then has developed into the structure of the normal mode. Detailed comparisons between the SV and NM structure in the various dynamic fields further bear this out (not shown).

Details of the SV exchange processes for the subcritical case $a = 0.9$ are shown in the lower panel of figure 4. At least in part these are in interesting correspondence to those seen in the constant-shear-layer approximation (Fig. 1). Buoyant energy exchange seems to trigger the energy growth. This is followed by a strong contribution $\Gamma_{\perp}$, indicating

that also here the roll mechanism is the most important process at work by which energy is transferred from the shear in the transverse wind component in the IGW (V_0) to the perturbation. In contrast to the predictions from the shear-layer approximation, however, there is no damped oscillation in the energy. This oscillation, a result of the repeated destructive and constructive interference between two damped normal modes, seems to be obstructed by the probably more complex modal decomposition of the SV in the more general approximation. One growth cycle is followed by decay which to about equal parts results from along-gradient momentum flux ($\Gamma_\perp$) and viscous-diffusive damping (Γ_d).

For an impression of the impact of the ratio M/K in the IGW we show for $a = 0.9$ and the vertical wavelengths $\Lambda_z = 3$ km and 9 km, but always $\Lambda_x = 500$ km, the time dependent growth-rate decomposition from integrations of the leading parallel SV in the left column of figure 6. In the shear-layer picture larger M/K means larger β and thus a more important contribution from the shear-related exchange term $\Gamma_\perp$ in comparison to Γ_b. Likewise one would expect an increase of the total growth factor and thus also the instantaneous growth rate. Both expectations are verified here while also in these cases no damped energy oscillation is observed.

The space-time dependence of the leading parallel SV for $(a, \Lambda_z) = (0.9, 6\text{km})$ is shown in figure 7 where on can see the time development (between $t = 0$ and $t = 2\tau$) of the real parts of all four model variables. At all stages the structure is extremely confined to the statically least stable altitude region, which might be an explanation why for this case the constant-shear-layer approximation works so reasonably. Notable is also the dominance of growth in $v_\perp$ (note the different contour intervals), resulting from the exchange via the roll mechanism, while the buoyancy perturbation is initially losing energy. The rapid

time-oscillation is due to the advection of the small-scale structure ($\lambda_\parallel \approx 660$ m) in the parallel wind in the IGW which reaches a minimum $U_0 \approx -11$ m/s at $z = 0$, also in agreement with the shear-layer picture (i.e. all variables are $\propto \exp\left(ik_\parallel U_\parallel t\right)$). The corresponding time development of the growth-rate contributions can be seen in figure 8, showing the strong exchange $\gamma_\perp$ due to the roll mechanism. It is interesting to see that the energy in b decays while γ_b is positive initially. This is a result of a buoyant exchange $\epsilon_{bw} = e_{bw}/\langle e_{kl}\rangle$ between the perturbation energy in b and w, while the latter then leads via $\gamma_\perp$ to the growth in $v_\perp$, showing how in this chain both reduced static stability (via γ_b) and the transverse wind shear (via $\gamma_\perp$) together lead to the strong overall growth of the perturbation in $v_\perp$. Note that $r_b = (1 - N_{tot}^2/N^2)\, e_{bw}$, implying that near the initially statically least stable altitude $z = 0$ buoyancy must necessarily decay via e_{bw} for $a < 1$ if $r_b > 0$. In fact figure 7 clearly shows that the energy in w increases if that in b decreases and vice versa.

4.1.2 Transverse SV

Now turning to the leading transverse SV we see in the right column of figure 4 energy for $a = 0.9$ and 1.1, and the growth-rate decomposition for $a = 0.9$, also from integrations over four optimization times. In contrast to the parallel case at the respective horizontal wavelength no unstable normal mode exists so that, as in the constant-shear-layer approximation, energy eventually decays. Details of the SV exchange processes for the subcritical case $a = 0.9$ are shown in the lower panel of figure 4. At least in part these are again in interesting correspondence to those seen in the constant-shear-layer approximation. Buoyant energy exchange seems to trigger the energy growth, followed by another contribution from $\Gamma_\parallel$, indicating the Orr mechanism to be at work, in which the

counter-gradient flux of $u_\parallel = v$ interacts with the corresponding shear $dU_\parallel/dz = dV_0/dz$ in the IGW. In contrast to the shear-layer approximation, however, there also is a final important contribution from $\Gamma_\perp$, so that also here the roll mechanism seems to be active. The impact of the ratio M/K in the IGW (right column in figure 6) is again in reasonable correspondence to the predictions from the constant-shear-layer approximation. Larger M/K, and hence larger β lead to a more important contribution from $\Gamma_\parallel$ in comparison to Γ_b, and also stronger overall growth. In all examined cases, however, we also see a significant contribution from the roll mechanism, as not predicted in the shear-layer picture.

The space-time dependence of the SV together with its energetics are shown in figures 9 and 10. Since $U_\parallel = V_0$ vanishes near $z = 0$ no corresponding high-frequent advection is visible as in the case of the parallel SV. A strong contribution from $\gamma_\parallel$ at $z = 0$ shows the Orr mechanism to work near the strongest gradient of $U_\parallel = V_0$. Similarly to the case of the parallel SV one finds, however, also a large initial γ_b while b decays, indicating that e_{bw} is immediately transferring buoyant energy into kinetic energy in w, thereby enforcing the roll mechanism which via $\gamma_\perp$ leads to a considerable increase in the energy in $v_\perp$. Note that the latter process here works at some distance from $z = 0$ where it would be forbidden due to $\partial V_\perp/\partial z = -\partial U_0/\partial z = 0$. The remaining behavior looks more complex, with apparent vertical radiation from the statically least stable altitude, ending in small-scale structures near $z = \pm\Lambda_z/2$ and $z = 0$. We also note that the vertical scales of the developing structures are progressively decreasing, leading to strong viscous-diffusive decay in the late stages of the development, and that they are considerably shorter than the ones set by the IGW packet. While the behavior near $z = 0$ is consistent with the picture of an

Orr mechanism leading to diverging vertical wave number in the source region, one might speculate that the development near $z = \pm\Lambda_z/2$ is relate to the approach of a small-scale wave towards a critical layer, as first described via WKB theory by Bretherton (1966). This is a hypothesis we want to test here in a quantitative manner.

We observe that in comparison to the perturbation the spatial and time dependence of the basic wave is weak. In the case of a constant background one would obtain from the model equations (see AS) plane gravity waves with no component in $v_\perp$. We therefore introduce a scaling parameter ε and use the modified WKB ansatz

$$\left(U_\parallel, V_\perp, N_{tot}^2\right)(z,t) = \left(\widetilde{U}_\parallel, \widetilde{V}_\perp, \widetilde{N_{tot}^2}\right)(\varepsilon z, \varepsilon t) \tag{31}$$

$$\left(u_\parallel, v_\perp, w, b, p\right)(z,t) = \left(\widetilde{u}_\parallel, \varepsilon\widetilde{v}_\perp, \widetilde{w}, \widetilde{b}, \widetilde{p}\right)(\varepsilon z, \varepsilon t)\, e^{i\eta(\varepsilon z, \varepsilon t)/\varepsilon} \quad . \tag{32}$$

We define

$$\omega = -\frac{1}{\varepsilon}\frac{\partial \eta}{\partial t} \tag{33}$$

$$m = \frac{1}{\varepsilon}\frac{\partial \eta}{\partial z} \quad , \tag{34}$$

while the model equations (neglecting the Coriolis effect) yield to lowest order in ε

$$u_\parallel = -i\frac{\widehat{\omega}}{N_{tot}^2}\frac{m}{k_\parallel}b \tag{35}$$

$$v_\perp = \frac{b}{N_{tot}^2}\frac{\partial V_\perp}{\partial z} \tag{36}$$

$$w = i\frac{\widehat{\omega}}{N_{tot}^2}b \tag{37}$$

$$\widehat{\omega} = \omega - k_\parallel U_\parallel = \delta\sqrt{\frac{N_{tot}^2 k_\parallel^2}{k_\parallel^2 + m^2}} \quad , \qquad \delta = \pm 1 \quad . \tag{38}$$

(33) – (34) can be combined with (38) to give a predictive equation for the local vertical wavenumber

$$\frac{\partial m}{\partial t} = -c_{gz}\frac{\partial m}{\partial z} - \frac{\partial \Omega}{\partial z} \tag{39}$$

with the vertical group velocity $c_{gz} = \partial\Omega/\partial m = -\widehat{\omega}m/\left(k_\parallel^2 + m^2\right)$ and the frequency function $\Omega\left(k_\parallel, m, z, t\right) = k_\parallel U_\parallel + \widehat{\omega}\left(k_\parallel, z, t\right)$. Once buoyancy b and the vertical wavenumber m have been diagnosed from the linear model one can examine whether $u_\parallel$, $v_\perp$, and w are for any δ consistent with the WKB theory via (35) – (37). Having verified this, it is then possible to go to (39) and identify the process responsible for the apparent increase of the vertical wavenumber in the layer formation. This is what we have done. The vertical wavenumber has been determined from the buoyancy fields by first determining $\exp\left(i\eta/\varepsilon\right) = b/\left|b\right|$ and hence $m = \Im\left[\exp\left(-i\eta/\varepsilon\right)\partial/\partial z \exp\left(i\eta/\varepsilon\right)\right]$.

For illustration we show some results for $z > 0$, while in the other altitude range our results support at the same accuracy the conclusions we come to here. For $t = 3\tau$ figure 11 shows the real and imaginary parts of the two horizontal wind components, as well as the prediction of these quantities from the basic-wave fields, b, and m, for both cases $\delta = \pm 1$. The time dependent vertical wavenumber and intrinsic frequency are shown in figure 12. One sees that $m < 0$ near $z = 0$ and $m > 0$ else. The agreement between the horizontal wind in the perturbation and the prediction from WKB theory is very good for $\delta = -1$ near $z = \Lambda_z/2$ and reasonable for $\delta = 1$ near $z = 0$. This indicates that the data can be interpreted by the WKB model as resulting from small-scale gravity waves radiating away from the statically least stable location.

Returning now to the critical-layer hypothesis we first note that local frequency $\omega\left(z,t\right) = \Omega\left[m\left(z,t\right), z, t\right]$ satisfies

$$\frac{\partial\omega}{\partial t} = -c_{gz}\frac{\partial\omega}{\partial z} + \frac{\partial\Omega}{\partial t} \qquad , \tag{40}$$

i.e. for a time-independent background frequency would be conserved along rays defined by the local group velocity. Under such circumstances a critical layer arises as in the course

of propagation along a ray $k_\parallel U_\parallel \to \omega$, and hence $\widehat{\omega} \to 0$ and $|m| \to \infty$. In (39) this should express itself in a dominance of $\partial\Omega/\partial z \approx k_\parallel \partial U_\parallel/\partial z$ on the right-hand side. Here we have a time-dependent background so that this picture can only be satisfied approximately. Still, however, we find the layer near $z = \Lambda_z/2$ to be characterized by an increase of vertical wavenumber and corresponding decrease of intrinsic frequency $\widehat{\omega}$, as visible in figure 12. In passing we also note the sign change in m near $z = 0$ from $t < \tau$ to $t > \tau$, as predicted from the shear-layer theory. In figure 13 we have finally plotted for the altitude $z = 0.45\Lambda_z$ the diagnosed tendency of vertical wavenumber (estimated from central 10-sec differences), the prediction of this by WKB theory, and the contribution to the latter by the vertical shear in the transverse wind of the basic IGW. Indeed WKB theory seems to give a useful approximation of the complete wavenumber dynamics during the formation of the small-scale layer. It slightly overestimates the wavenumber increase but the basic effect is reproduced, where it is mostly the vertical shear in $U_\parallel = V_0$ which causes the scale collapse observed at the shear layer. In summary, although the time-dependence of the background precludes a robust critical layer (see also Broutman and Young, 1986), we see a strongly related effect due to the propagation of the excited perturbation towards the zero lines $z = \pm\Lambda_z/2$ of transverse wind in the basic IGW packet.

4.2 Long optimization times

In our analysis of SV for longer optimization times we have focussed again on the sub-critical case $(a, \Lambda_z) = (0.9, 6\text{km})$. For all calculations we used a model resolution of 1024 grid points/$5\Lambda_z$, where the model domain size was always chosen large enough so that potentially radiating structures (see below) never reached the model boundaries. Exam-

ined optimization times are $\tau = 1\text{h}, 2\text{h}, 5\text{h}$, and 10h. The last value approaches the IGW period $T \approx 11\text{h}$. The time dependence of the wave packet makes the results from the constant-shear-layer approximation the less applicable the larger τ/T is. The nicer it is to see how much it can still be used for qualitative explanations of SV behavior in these cases.

Figure 14 shows the wavelength dependent growth-factor curves. In agreement with the expectations from the constant-shear-layer theory (see AS) the singular vectors are to be found at progressively increasing wavelengths as τ is increased. At large τ, however, for all azimuth angles an important growth-factor peak at rather short scales (of the order Λ_z) appears with values as large as nearly 50 at $\alpha = 30°$ for $\tau = 10$ h. Another prediction we find verified is that the largest growth factor at $\alpha = 0°$ is approximately independent of τ, i.e. $\sigma_1^2 \approx (4/\text{Ri})\,(N^2/N_{tot}^2) \approx 238$ as determined from the conditions at the statically least stable altitude. Also as expected, at least for intermediate τ transverse optimal growth gets larger than its parallel counterpart. Most important at large τ are, however, oblique azimuth angles, which dominate at nearly all scales. For these cases neither the statically enhanced roll or Orr mechanisms act alone but always a combination of the two.

For $\tau = 2$ h we show in figure 15 the time dependent growth-rate decomposition for the optimally growing structure at each of the four examined azimuth angles. The behavior of the parallel optimal perturbation is still very similar to the one at short optimization times, albeit on a longer time scale. Again we see the statically enhanced roll mechanism at work, with an initial trigger by buoyancy related energy exchange with the IGW. $\Gamma_\parallel$ rises at larger α in importance over $\Gamma_\perp$, while the initial contribution from Γ_b is always there, giving an indication of a statically enhanced Orr mechanism. Again we do not see

the damped energy oscillation from the constant-shear-layer picture at $\alpha = 0°$. At $\alpha > 0°$ damped oscillatory behavior is visible, but from the next two figures one can see that the process behind this is not the same as in the shear-layer approximation.

In figure 16 one can see for all azimuth angles the development of the real part of the vertical wind in the perturbation, while figure 17 shows for $\alpha = 60°$ the space-time dependence of the four growth-rate contributions. One sees that for all $\alpha < 90°$ the singular vectors radiate small-scale gravity waves into the far field where the IGW does not influence the propagation conditions any more. In figure 17 one can recognize that the damped oscillatory behavior of the growth-rate contributions results from the movement of the radiated waves through the IGW. In the course of this propagation it gets successively into contact with differing shear and stratification conditions. As static energy exchange Γ_b is only important initially it is concentrated in the packet center, but the shear-related exchange terms $\gamma_\parallel$ and $\gamma_\perp$ are correlated with the respective gradients $\partial U_\parallel/\partial z$ and $\partial V_\perp/\partial z$. The corresponding oscillation in the energy exchange (Fig. 15) gets weaker as the radiated waves move away from the center of the IGW packet into regions where the IGW gradients are negligible.

It is interesting to note that the fact that we here find wave radiation by the SV, while this is not to be seen for the shorter optimization time $\tau = 10$ min (see figures 7 and 9), can be understood in terms of simple linear gravity-wave dynamics. As shown above, but also visible in figure 16, all but the transverse singular vectors show a rapid time oscillation in all fields with a period determined by advection of their small-scale structure in the wind $U_\parallel$ in the IGW near the statically least stable location, i.e. their frequency is $\omega \approx k_\parallel U_\parallel$. In the external region (where the IGW fields are essentially zero)

gravity waves at such a frequency can only propagate if $|\omega| < N$ so that non-evanescent wavenumbers are limited to $k_\parallel < N/\left|U_\parallel\right|$. Since the scales of SV at short optimization times are too small for this (e.g. $\lambda_\parallel \approx 660$ m for $\alpha = 0°$ and $\tau = 10$ min, see AS) they cannot radiate, while the opposite holds for longer τ. The same rationale can also explain the vertical scales of the radiated structures themselves. From the far-field gravity-wave dispersion relation $\omega = \pm N k_\parallel / \sqrt{k_\parallel^2 + m^2}$ follows for $\alpha < 90°$ (neglecting the Coriolis effect)

$$m = \sqrt{\frac{N^2}{u_0^2 \cos^2 \alpha} - k_\parallel^2} \qquad , \tag{41}$$

since near the statically least stable location $U_\parallel = u_0 \cos\alpha$. From this relation we find for the radiated structures in figure 17 the predicted vertical scales $2\pi/m \approx 2.7\Lambda_z, 1.1\Lambda_z, 0.61\Lambda_z$ for $\alpha = 0°, 30°, 60°$, where the optimal wavelengths are 7.9 km, 16 km, and 16 km, respectively (see Fig. 14) . These are in quite good agreement with the numerical results shown here. As a consequence one can expect as far-field behavior of slightly subcritical IGW the radiation of high-frequent gravity waves with increasingly shorter periods and longer vertical wavelengths as the azimuth angle decreases. From the same reasoning one can also expect transverse radiation to be basically obstructed, since the resulting waves will always be evanescent.

It is noteworthy that even for $\tau = 10$ h the growth factor is near 50. The time the corresponding perturbations take for their amplification is quite large so that their appearance might be prevented by nonlinear modifications of the IGW under the influence of other perturbations rising in amplitude more quickly. The oblique propagation directions of these SV, however, suggest that they are relate to the diagonal shear modes found by Lelong and Dunkerton (1998a) in their simulations of a case with $a = 0.95$ and a ratio

between inertial frequency and IGW frequency $R = 0.7$, which is rather near to our combination $(R, a) = (0.65, 0.9)$. A one-two-one comparison is difficult since in that study an artificially increased ratio $f/N = 0.1$ was used, but it is striking that there an asymmetry in perturbation growth about $\alpha = 90°$ was found, so that if our findings were relate to that work, we should also see a corresponding asymmetry in the growth factors. Indeed this is the case. So we find that SV growth over $\tau = 10$ h is not larger than by a factor 9 if determined for the azimuth angles $\alpha = 120°$ and $150°$ (not shown here). Moreover, those authors also found a vacillation of energy growth about a mean value. This seems to be relate to the damped vacillation we find, as e.g. in figure 15 but also visible for other τ than 2 h, which is due to the movement of the perturbation through the periodic IGW fields.

5 SV in the general IGW packet

Dropping all simplifications we finally get to the most general SV in the IGW packet with complete time and space dependence. As discussed above these are of the form $(\mathbf{v}', b', p') = (\mathbf{v}, b, p)\,(x, z)\exp(ily)$ with an arbitrary wavenumber $l = 2\pi/\lambda_y$ in y-direction. One would expect that in a survey of the SV dependence on λ_y the parallel SV from above leave their traces among the general SV for $\lambda_y = \infty$, whereas oblique and transverse SV are to be found among $\lambda_y < \infty$. For illustration we here discuss the two cases $\tau = 10$min and 1h for $a = 0.9$ each[2]. For the wavelength range between $\lambda_y = 1$km and 6 km the growth

[2]Expecting the resulting features to be located near the location of least static stability the IGW packet, from a nonlinear integration in a periodic box with dimensions $(L_x, L_z) = (\Lambda_x, 5\Lambda_z) = (500\text{km}, 30\text{km})$, was stored for greater numerical efficiency for the analyzes of $\lambda_y < \infty$ in the inner sub-domains with $(L_x, L_z) = (\Lambda_x/2, 3\Lambda_z)$ and tapered to zero with a cosine profile in the outer regions

factors we found for the leading SV are shown in figure 18. One sees for $\tau = 10$min a local optimum with growth by $\sigma_1 = 6.8$ at $\lambda_y = 3.9$km. This seems to be relate to optimal transverse growth, i.e. at $\alpha = 90°$, in the 1-D profile by $\sigma_1 = 7.0$ at $\lambda_\parallel = 3.8$ km (see AS). For the same τ the general SV at $l = 0$ grows by $\sigma_1 = 8.9$, just as the leading parallel SV, i.e. for $\alpha = 0°$, we found for the 1-D profile in AS. The wavelength $\lambda_\parallel = 660$ m of that pattern also is in good agreement with the scales of the general SV (see below). For $\tau = 1$ h we find an optimum at $(\lambda_y, \sigma_1) = (5.5\text{km}, 26.3)$ which seems to correspond to optimal transverse growth in the 1-D approximation at $\left(\lambda_\parallel, \sigma_1\right) = (5.0\text{km}, 24.1)$. At $l = 0$ we find optimal growth by $\sigma_1 = 14.7$, seemingly corresponding to the leading parallel SV in the 1-D approximation at $\left(\lambda_\parallel, \sigma_1\right) = (7.1\text{km}, 13.7)$. Also here the scales of the general SV and the one from the 1-D approximation are in good agreement (not shown).

Also the energetics of the identified patterns indicates their relation to the SV from the 1-D approximation. In general one can derive for the energy density $e_l = 1/2\left(|\mathbf{v}|^2 + |b|^2/N^2\right)$

$$\frac{\partial e_l}{\partial t} + \nabla_y \cdot \left[\mathbf{V}_0 e_l + \Re\left(\overline{\mathbf{v}} p\right) - \nu \nabla_y \frac{|\mathbf{v}|^2}{2} - \mu \nabla_y \frac{|b|^2}{2N^2}\right] = r_u + r_v + r_w + r_b - D_v - D_b \quad (42)$$

with

$$r_u = -\Re\left(u\overline{\mathbf{v}}\right) \cdot \nabla_y U_0 \quad (43)$$

$$r_v = -\Re\left(v\overline{\mathbf{v}}\right) \cdot \nabla_y V_0 \quad (44)$$

$$r_w = -\Re\left(w\overline{\mathbf{v}}\right) \cdot \nabla_y W_0 \quad (45)$$

therefrom with horizontal extent $\Lambda_x/8$ and vertical extent Λ_z. For $\tau = 10$min and $l = 0$ the stored inner sub-domain is of extent $(L_x, L_z) = (\Lambda_x/2, \Lambda_z)$ with tapering over the horizontal extent $\Lambda_x/8$ and over the vertical extent $\Lambda_z/8$, while for $\tau = 1$h and $l = 0$ the stored inner sub-domain is of extent $(L_x, L_z) = (\Lambda_x/2, 5\Lambda_z)$ with tapering over the horizontal extent $\Lambda_x/8$. In each case the chosen resolution was made sure to well resolve all essential resulting features. In several experiments it was also made sure that the limitation to the central least stable region was of no effect on the results

$$r_b = -\Re\left(b\overline{\mathbf{v}}\right)\cdot\frac{1}{N^2}\nabla_y B_0 \tag{46}$$

$$D_v = \nu\left[l^2\left|\mathbf{v}\right|^2+\sum_{i=1}^{3}\left|\nabla_y v_i\right|^2\right] \tag{47}$$

$$D_b = \frac{\mu}{N^2}\left[l^2\left|b\right|^2+\left|\nabla_y b\right|^2\right] \quad , \tag{48}$$

where $\nabla_y = (\partial/\partial x, 0, \partial/\partial z)$. Energy exchange between w and b is given by the same term e_{bw} as in (28). As before we calculate from the exchange terms corresponding instantaneous growth rate contributions Γ_u etc. For $\tau = 10$ min and $a = 0.9$ we show the time-dependence of these and total energy in the identified SV in figure 19. The latter is split into kinetic energy $E_{kin} = \int dxdz\left|\mathbf{v}\right|^2/2$ and available potential energy $E_{pot} = \int dxdz\left|b\right|^2/2N^2$. The negligible contribution from Γ_w is not shown. Comparison with figure 4 further stresses the similarity between the general SV and the ones from the analysis of the 1-D profile, where for the case $\lambda_y = \infty$ or $\alpha = 0°$ one obviously has to compare Γ_u with $\Gamma_\parallel$ and Γ_v with $\Gamma_\perp$, while in the case $\lambda_y = 3.8$ km or $\alpha = 90°$ the corresponding pairs are Γ_u and $\Gamma_\perp$, and Γ_v and $\Gamma_\parallel$. It thus is also no surprise that closer inspection also shows that in the general case the gradients in x-direction do not contribute to the energy budget in any significant way (not shown). Similar conclusions also hold for the case $\tau = 1$ h (also not shown).

Of largest remaining interest therefore is the horizontal distribution of the general SV, since the horizontal limitation of the statically weakly stable location should be expected to have some impact. Indeed we find this to be the case. Figure 20 shows for $\tau = 10$ min the leading SV at $l = 0$ and at $t = \tau$ in the region where it has significant amplitude. One observes that it is a wave packet both vertically and horizontally closely confined near the location of least static stability. In the course of the time integration we observe its rapid leftwards advection to smaller x by the U_0-wind in the IGW (not shown). Note

that near $a = 1$ this advection is approximately at the horizontal phase velocity of the IGW so that the SV follows the movement of the statically least stable location, thereby enabling longer transient growth. Also here the overwhelming contribution to this growth is from the amplification of v. For $\tau = 10$ min and $\lambda_y = 3.8$ km we show in figure 21 the time development of buoyancy in the leading SV between $t = 0$ and $t = 3\tau$. Once again one finds it to be confined to the location of least static stability, but of larger extent than the patterns at $l = 0$. This is consistent with the expectation, from the 1-D picture, of a structure with comparatively weaker dependence on x than on y. Clearly visible is also the critical-layer behavior near the zero lines of V_0. Our observations for $\tau = 1$h are quite analogous (not shown). Also these patterns are closely confined to the region of least static stability. The structure at $l = 0$ is advected by U_0 towards smaller x, thereby following the least stable location. As was to be expected from the previously said we also find it to radiate small-scale gravity waves into the exterior range not affected by the IGW where they can propagate freely. Also as expected, the more strongly growing structure at $\lambda_y = 5.5$ km cannot radiate but exhibits similar critical-layer behavior near the zero-lines of V_0 as visible in figure 21.

6 Summary and discussion

In our pair of studies (the present and AS) of optimal perturbations to IGW packets in the mesosphere we have worked ourselves upwards through a hierarchy of three models with increasing complexity, each of them providing instructive pieces of information to the whole picture we have by now. It is pleasing to recognize that many features can already be understood on the basis of a stratified constant-shear-layer approximation where only

the local stratification and transverse-wind gradient $\partial V_0/\partial z$ near the statically least stable location of the IGW packet enter. Based on previous relate work by Farrell and Ioannou (1993a,b) and Bakas et al. (2001) it is found that the two cases of perturbations most accessible to closed analytic treatment, i.e. propagating in the horizontal parallel (i.e. at azimuth angle $\alpha = 0°$) or transverse ($\alpha = 90°$) with respect to the IGW, can be understood in terms of a roll or Orr mechanism, respectively, both controlled by the shear, however significantly amplified by the locally reduced static stability. The latter serves as a catalyst for buoyant energy exchange between IGW and vertical wind in the perturbation, thus further enforcing the shear-related exchange processes.

The SV energetics in an approximation of the IGW by its time dependent vertical profile at the horizontal location $x = \Lambda_x/2$ with initially least static stability basically reproduces these findings. It further highlights a basic distinction between NM and SV that the former are structurally fixed while the latter can adjust their fields instantaneously so that over a finite time a more efficient energy exchange with the IGW is possible than in the NM case, thus giving a further explanation of the more rapid transient growth of SV than admitted for NM. The 1-D approximation of the IGW fields also shows the close initial confinement of the optimal perturbation to the altitude of least static stability. For *short optimization times* the leading parallel SV, having an intrinsic short time scale set by the advection of its small-scale fields by the parallel horizontal wind in the IGW, stays there as it is prevented from outwards radiation by a linear wave duct. Similar observations hold for oblique SV which at fixed optimization time have progressively larger intrinsic time scales as the azimuth angle increases. The leading transverse SV is characterized by intermediate radiation away from its origin, with further energy growth via

a roll mechanism where an IGW shear in the parallel horizontal wind component exists, until its further vertical propagation is blocked by a critical-layer interaction at the zero line of the transverse wind in the IGW.

Similar behavior is also found in the most general treatment of the problem where also the horizontal spatial dependence of the IGW is taken into account. The SV from the 1-D approximation are basically reproduced, then however with a horizontal modulation of their amplitude so that they tend to be confined to the statically least stable horizontal location. From this one can expect a certain patchiness in the turbulence onset in an IGW packet propagating upwards through the mesosphere, as would be consistent with turbulence measurements from rocket soundings (Müllemann et al., 2003). It also is not in disagreement with relate simulations of IGW breakdown by Lelong and Dunkerton (1998a,b) who show turbulence onset to be confined to the phase of static least stability in their monochromatic wave.

While the energy growth of parallel SV is favored for short optimization times, it is also limited from above by $(4/\mathrm{Ri})\,(N^2/N_{tot}^2)$, so that *for larger optimization times* oblique and transverse SV prevail. The time scale of the long-term transient growth behavior of all SV, ending in algebraic or viscous-diffusive decay when no growing normal mode exists, but exhibiting asymptotic convergence towards the leading unstable NM if there is any, is to the most part set by τ, so that for a wide range of optimization times considerable optimal growth is allowed. As the optimization time is increased both the dominant spatial and intrinsic time scales of the identified perturbations get larger, and for optimization times approaching the IGW period transient growth by an amplitude factor as large as 50 is still observed. The oblique SV found there might be relate to the diagonal shear modes

diagnosed by Lelong and Dunkerton (1998a) in their simulations of the breakdown of a statically stable IGW.

Another interesting result is the observation that SV for longer optimization times tend to radiate gravity waves into the exterior field where the IGW has no direct impact any more. This offers an alternative mechanism for a mesospheric gravity wave source to the excitation of gravity waves by ageostrophic body forcing resulting from gravity-wave breakdown (Vadas and Fritts, 2001; Zhou et al., 2002) or by normal-mode instabilities of statically unstable IGW (Kwasniok and Schmitz, 2003). Specific features of the radiation mechanism identified by us are that it does not require the basic IGW to be unstable in the normal-mode sense and that the vertical wavelength and the frequency of the radiated waves get larger the more parallel the propagation direction of the radiated waves is with respect to the IGW.

Still we think that it is two early to decide how relevant SV are on the whole for the problem of turbulence onset in breaking IGW. In the end one might find that the answer is case-dependent, so that for the propagation of an IGW packet into a medium already left rather turbulent from a previous breaking event short-term growth of SV might be more important for describing the turbulence amplification in the IGW, whereas the IGW breaking in a rather quiescent medium, allowing the perturbations a free linear development over an IGW period or longer, might be more similar to predictions from normal-mode theory. For this further analyzes and simulations of IGW breaking initialized from growing NM or SV seem necessary which are, however, beyond the scope of this paper.

Acknowledgements

The authors thank two anonymous reviewers for numerous helpful suggestions for an improvement of the original manuscript.

References

Achatz, U., and G. Schmitz, 2005: Shear and static instability of inertia-gravity wave packets: Short-term modal and nonmodal growth. *J. Atmos. Sci.*, submitted

Bakas, N.A., Ioannou, P.J., and G.E. Kefaliakos, 2001: The emergence of coherent structures in stratified shear flow. *J. Atmos. Sci.*, **58**, 2790-2806

Bretherton, F.P., 1966: The propagation of groups of internal gravity waves in a shear flow. *Quart. J. Roy. Met. Soc.*, **92**, 466-480

Broutman, D., and W.R. Young, On the interaction of small-scale oceanic internal waves with near-inertial waves, *J. Fluid Mech.*, **166**, 341-358 (1986)

Dunkerton, T.J., 1997: Shear instability of internal inertia-gravity waves. *J. Atmos. Sci.*, **54**, 1628-1641

Farrell, B.F., 1988a: Optimal excitation of neutral Rossby waves. *J. Atmos. Sci.*, **45**, 163-172

Farrell, B.F., 1988b: Optimal excitation of perturbations in viscous shear. *Phys. Fluids*, **31**, 2093-2102

Farrell, B.F., and P.J. Ioannou, 1993a: Transient development of perturbations in stratified shear flow. *J. Atmos. Sci.*, **50**, 2201-2214

Farrell, B.F., and P.J. Ioannou, 1993b: Optimal excitation of three-dimensional perturbations in viscous constant shear flow. *Phys. Fluids A*, **5**, 1390-1400

Fritts, D.C., and L. Yuan, 1989: Stability analysis of inertio-gravity wave structure in the middle atmosphere. *J. Atmos. Sci.*, **46**, 1738-1745

Fritts, D.C., C. Bizon, J.A. Werne, and C.K. Meyer, 2003: Layering accompanying turbulence generation due to shear instability and gravity-wave breaking. *J. Geophys. Res.*, **108**, 8452, doi:10.1029/2002JD002406

Kwasniok, F., and G. Schmitz, 2003: Radiating instabilities of internal inertio-gravity waves. *J. Atmos. Sci.*, **60**, 1257-1269

Lelong, M.-P., and D.J. Dunkerton, 1998a: Inertia-gravity wave breaking in three dimensions. Part I: Convectively stable waves. *J. Atmos. Sci.*, **55**, 2473-2488

Lelong, M.-P., and D.J. Dunkerton, 1998b: Inertia-gravity wave breaking in three dimensions. Part II: Convectively unstable waves. *J. Atmos. Sci.*, **55**, 2489-2501

Lübken, F.-J., 1997: Seasonal variation of turbulent energy dissipation rates at high latitudes as determined by in situ measurements of neutral density fluctuations. *J. Geophys. Res.*, **102**, 13441-13456

Müllemann, A., M. Rapp, and F.-J. Lübken, 2003: Morphology of turbulence in the polar summer mesopause region during the MIDAS/SOLSTICE campaign 2001. *Adv. Space Res.*, **31**, 2069-2074

Tapp, M.C., and P.W. White, 1976: A non-hydrostatic mesoscale model. *Quart. J. Roy. Meteor. Soc.*, **102**, 277-296

Vadas, S.L., and D.C. Fritts, 2001: Gravity wave radiation and mean responses to local body forces in the atmosphere. *J. Atmos. Sci.*, **58**, 2249-2279

Yau, K.-H., G.P. Klaassen, and L.J. Sonmor, 2004: Principal instabilities of large amplitude inertio-gravity waves. *Phys. Fluids*, **16**, 936-951

Yuan, L., and D.C. Fritts, 1989: Influence of a mean shear on the dynamical instability of an inertia-gravity wave. *J. Atmos. Sci.*, **46**, 2562-2568

Zhou, X., Holton, J.R., and G.R. Mullendore, 2002: Forcing of secondary waves by breaking of gravity waves in the mesosphere. *J. Geophys. Res.*, **107**, doi:10.1029/2001JD001204

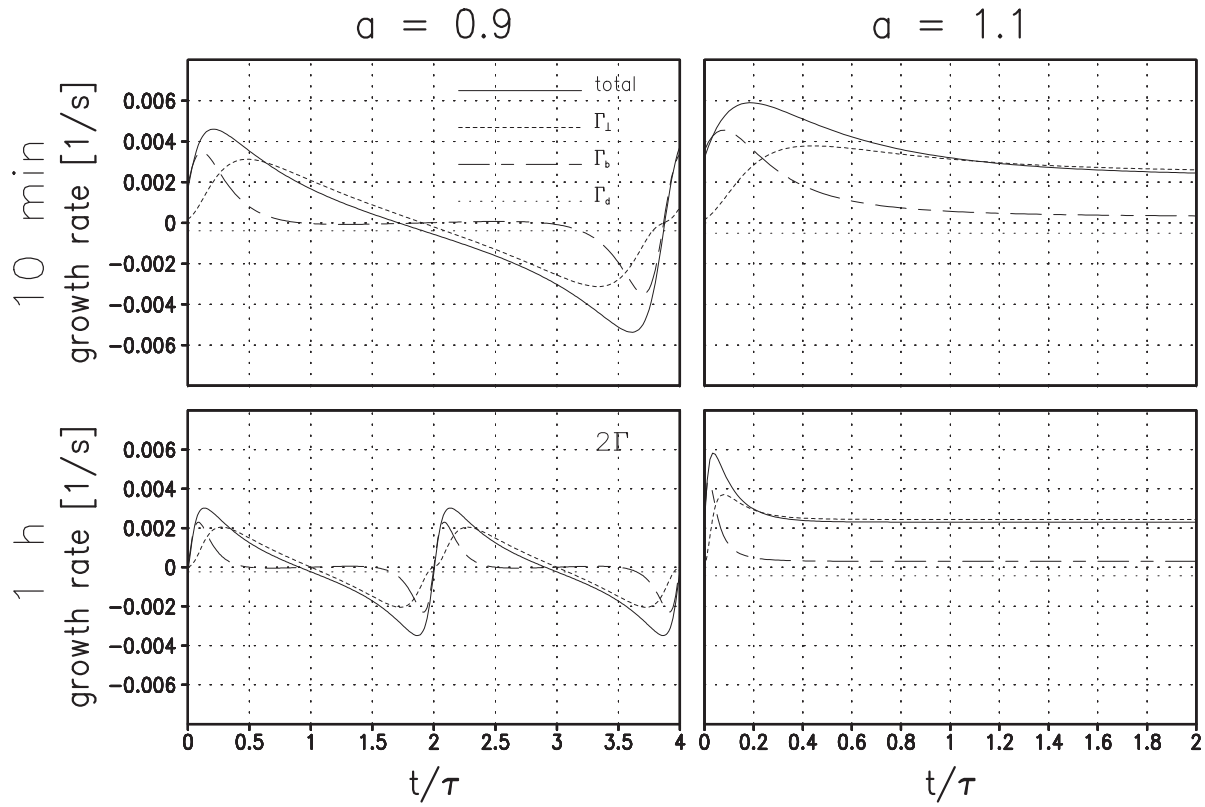

Figure 1: For the shear-layer approximation of optimal growth of parallel perturbations ($\alpha = 0$, vertical wavelength $\lambda_z = 600$ m) in an IGW packet ($\Lambda_z = 6$ km) with two different amplitudes a the time-dependent growth-rate decomposition from an integration of the leading optimal perturbation (i.e. at optimal horizontal wavenumber) for optimization times $\tau = 10$ min and 1 h. The contributing terms are the instantaneous growth rates due to vertical counter-gradient fluxes of momentum in $y_\perp$-direction and buoyancy b, and viscous and diffusive damping. For the case $(a, \tau) = (0.9, 1\text{h})$ we show twice the growth rates.

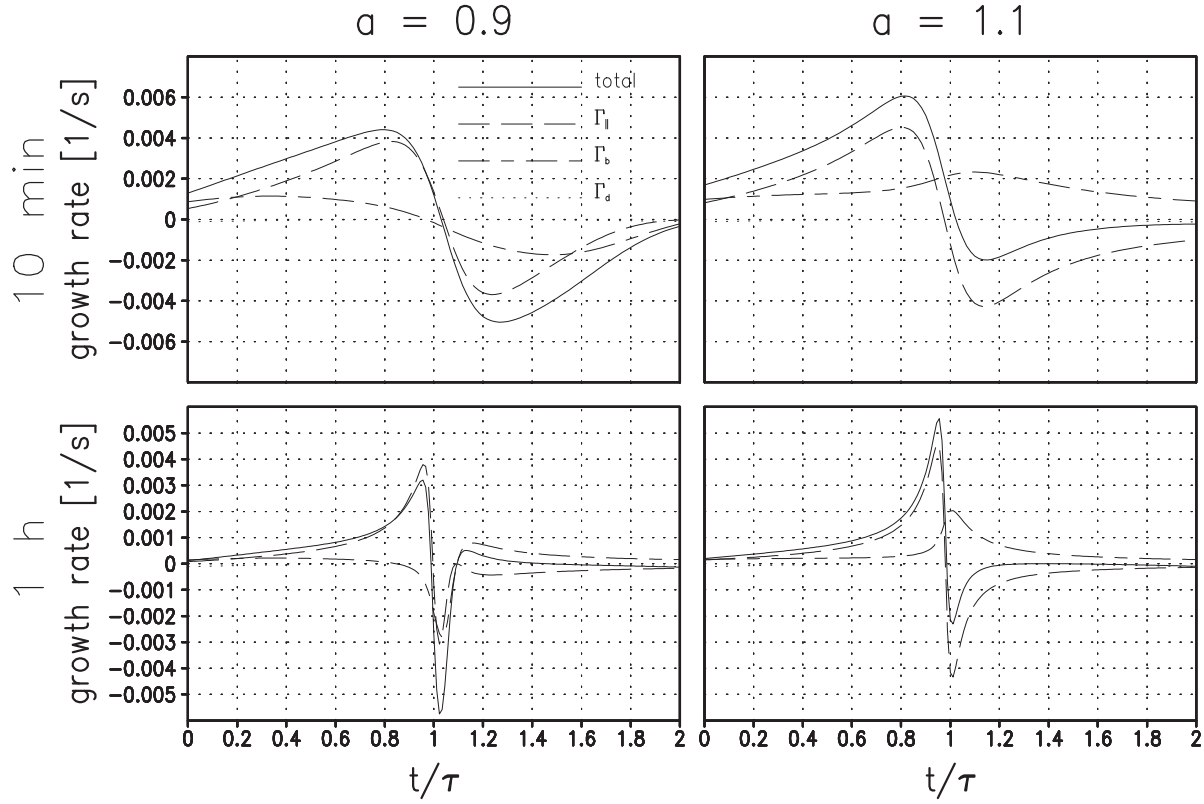

Figure 2: As Fig. 1, but now for the leading transverse perturbations ($\alpha = 90°$). Instead of the counter-gradient flux of momentum in $y_\perp$-direction one here has a contribution from the flux of momentum in $x_\parallel$-direction.

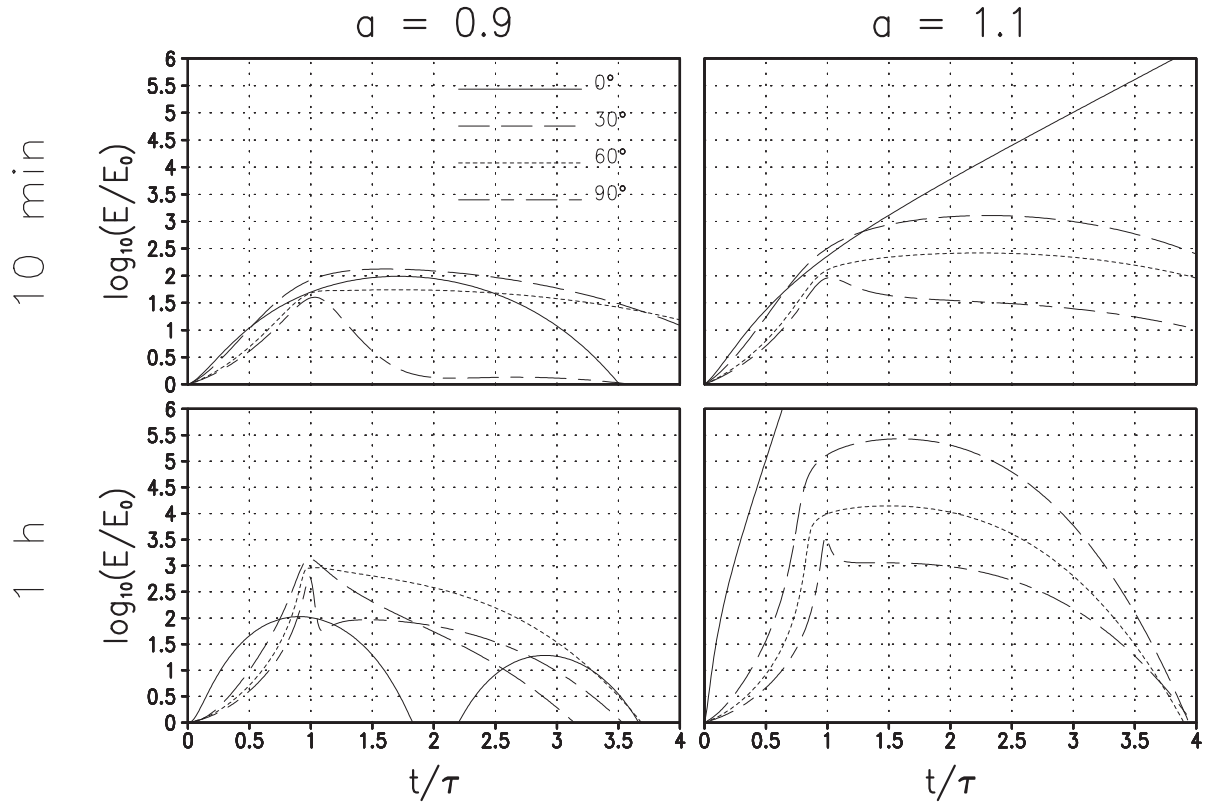

Figure 3: For the same four combinations of a and τ and the same λ_z and Λ_z as in figure 1 the time-dependent energy in the integration of the leading optimal perturbations for the azimuth angles $\alpha = 0°, 30°, 60°$, and $90°$.

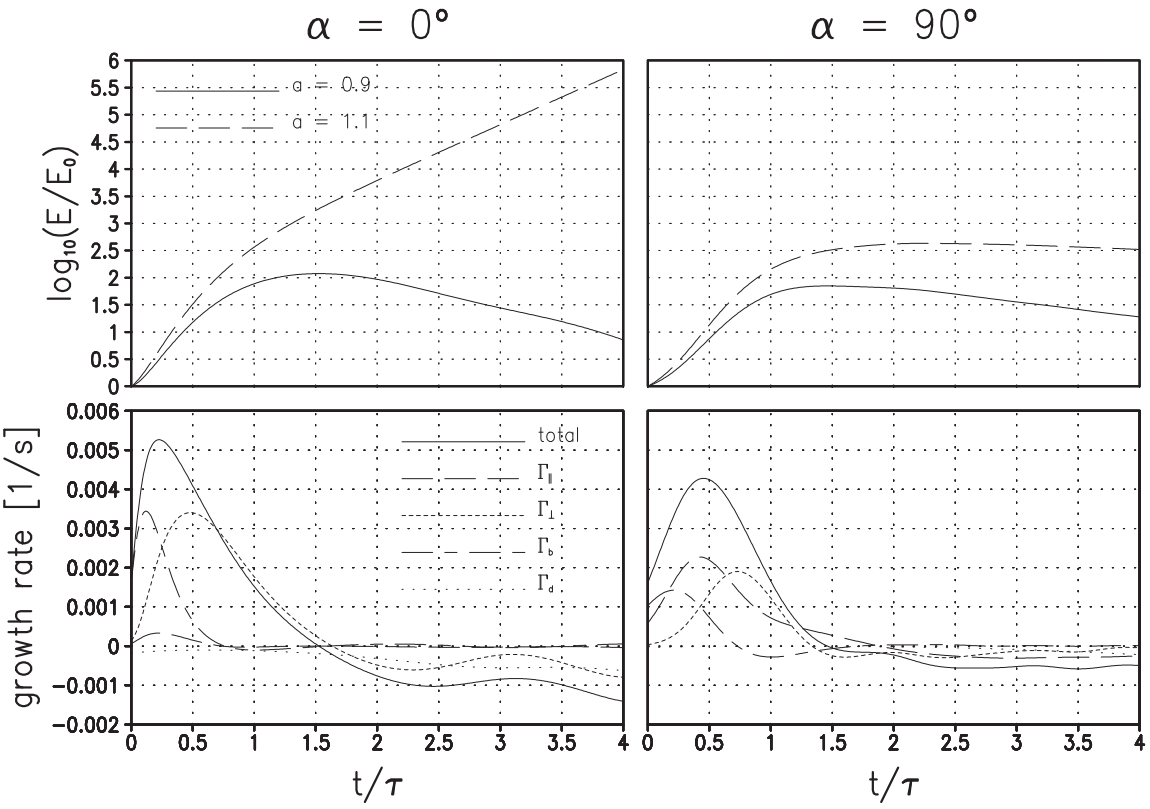

Figure 4: For the leading (i.e. at optimal horizontal wavelength) parallel SV (left column) and transverse SV (right column) in the approximation of the IGW with $\Lambda_z = 6$ km by a 1-D profile, time-dependent total energy for $a = 0.9$ and $a = 1.1$ (top row) and for $a = 0.9$ the instantaneous growth rate and its decomposition (bottom), from integrations over four optimization periods $\tau = 10$ min.

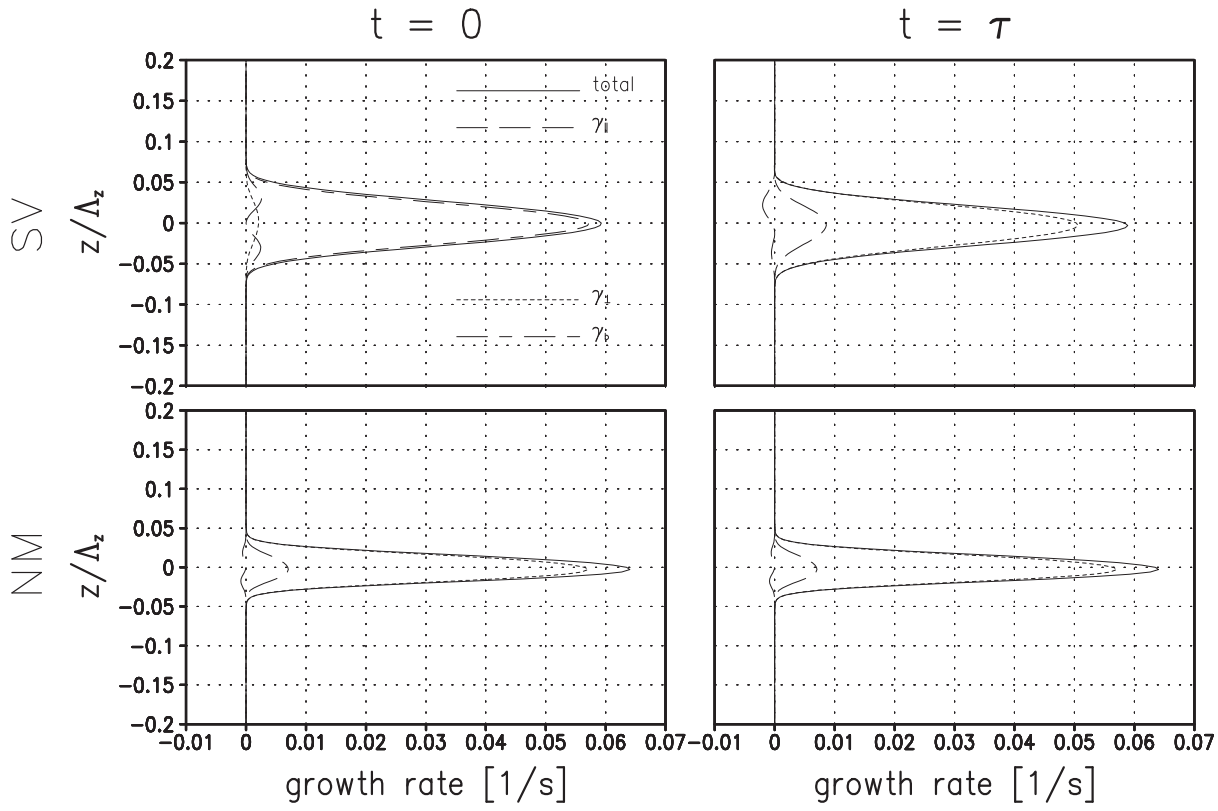

Figure 5: For the 1-D-profile approximation of an IGW with $(a, \Lambda_z) = (1.1, 6\text{km})$, the altitude-dependent growth-rate decomposition at $t = 0$ (left column) and $t = \tau$ (right) for the leading SV (i.e. at the optimal horizontal wavelength) for optimization time $\tau = 10$ min (top row), and the leading normal mode at the same horizontal wavelength (bottom).

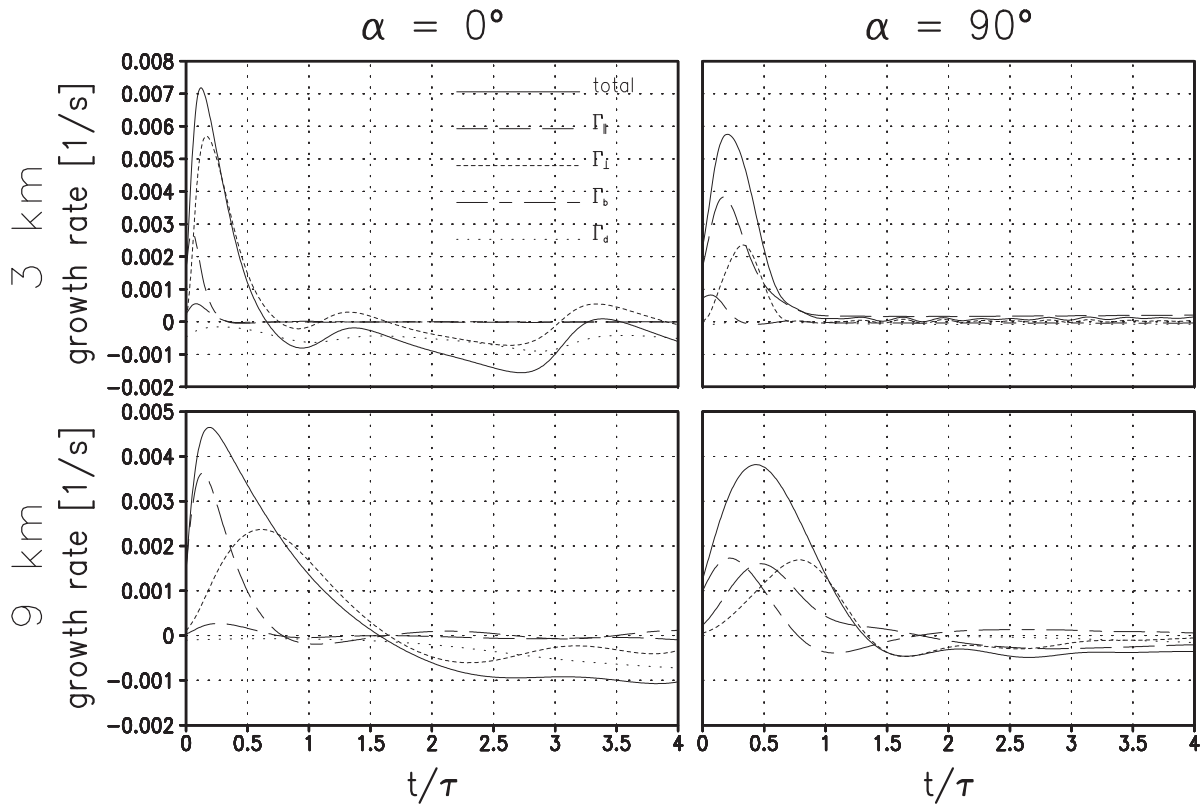

Figure 6: As the bottom row in Fig. 4, but now for $\Lambda_z = 3$ km (top row here) and $\Lambda_z = 9$ km (bottom).

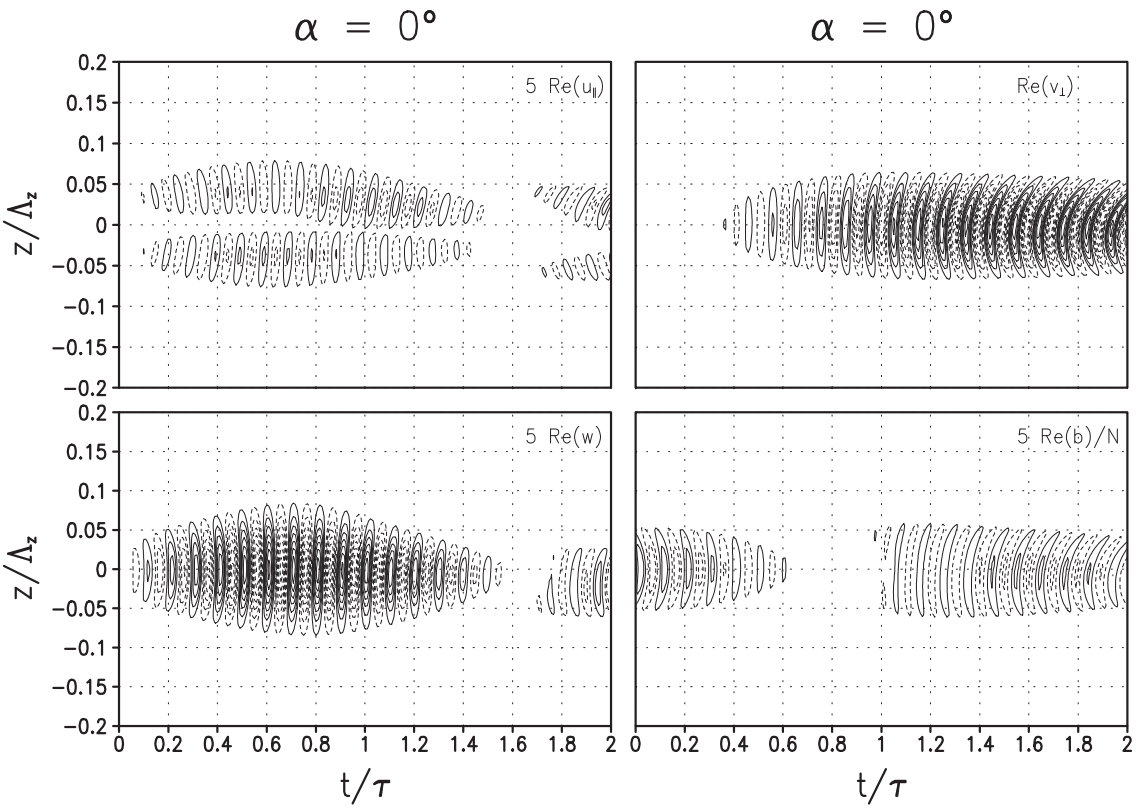

Figure 7: For the leading (i.e. at optimal horizontal wavelength) parallel SV in the approximation of the IGW with $\Lambda_z = 6$ km and $a = 0.9$ by a 1-D profile, the time-dependent real parts of all four model variables from integrations over two optimization periods $\tau = 10$ min. Contour intervals are in arbitrary units, but five times larger for $v_\perp$ than for the other variables. The zero contour is not shown. Negative values are indicated by dashed contours.

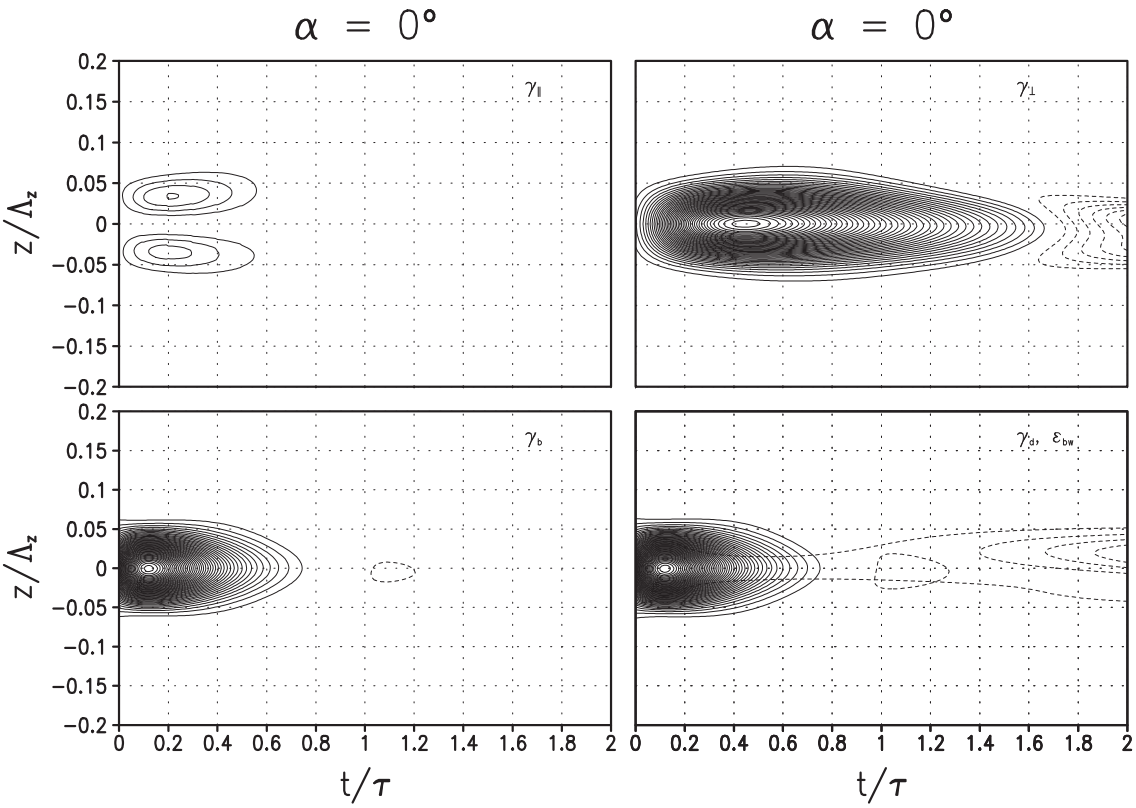

Figure 8: For the same integration as shown in Fig. 7 the corresponding altitude-dependent growth-rate contributions. The contour interval is $2 \cdot 10^{-4} \mathrm{s}^{-1}$. The zero contour is not shown. Negative values are indicated by dashed contours. In the lower right panel the viscous-diffusive damping is recognizable from its negative values throughout.

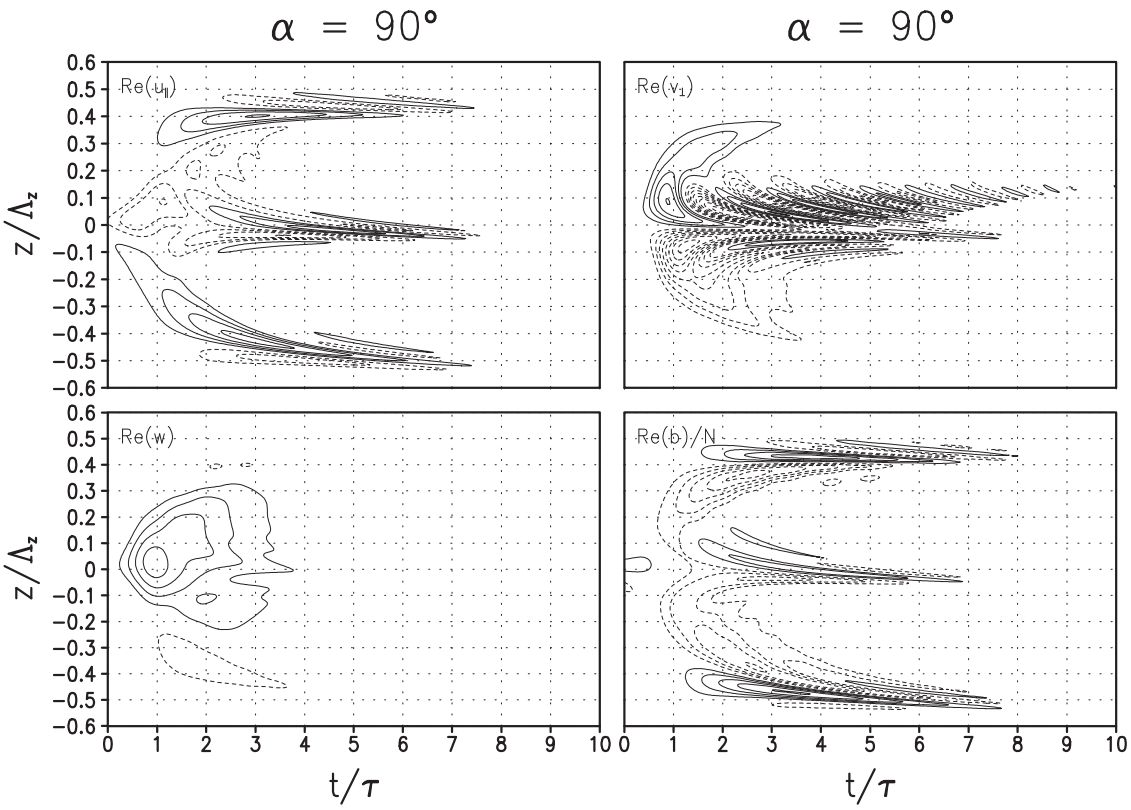

Figure 9: As Fig. 7, but now from an integration of the leading transverse SV over ten optimization periods $\tau = 10$ min. Here all variables are shown with identical contours.

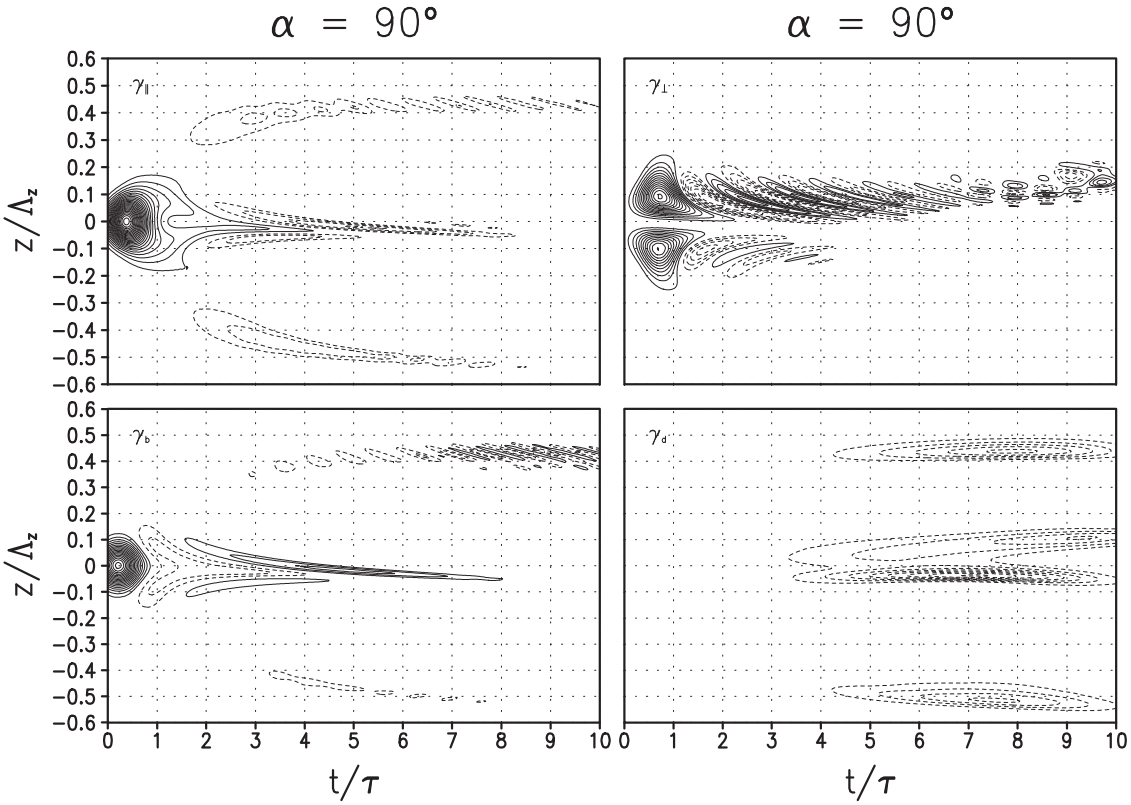

Figure 10: For the same integration as shown in Fig. 9 the corresponding altitude-dependent growth-rate contributions. The contour interval is $2 \cdot 10^{-4} s^{-1}$. The zero contour is not shown. Negative values are indicated by dashed contours.

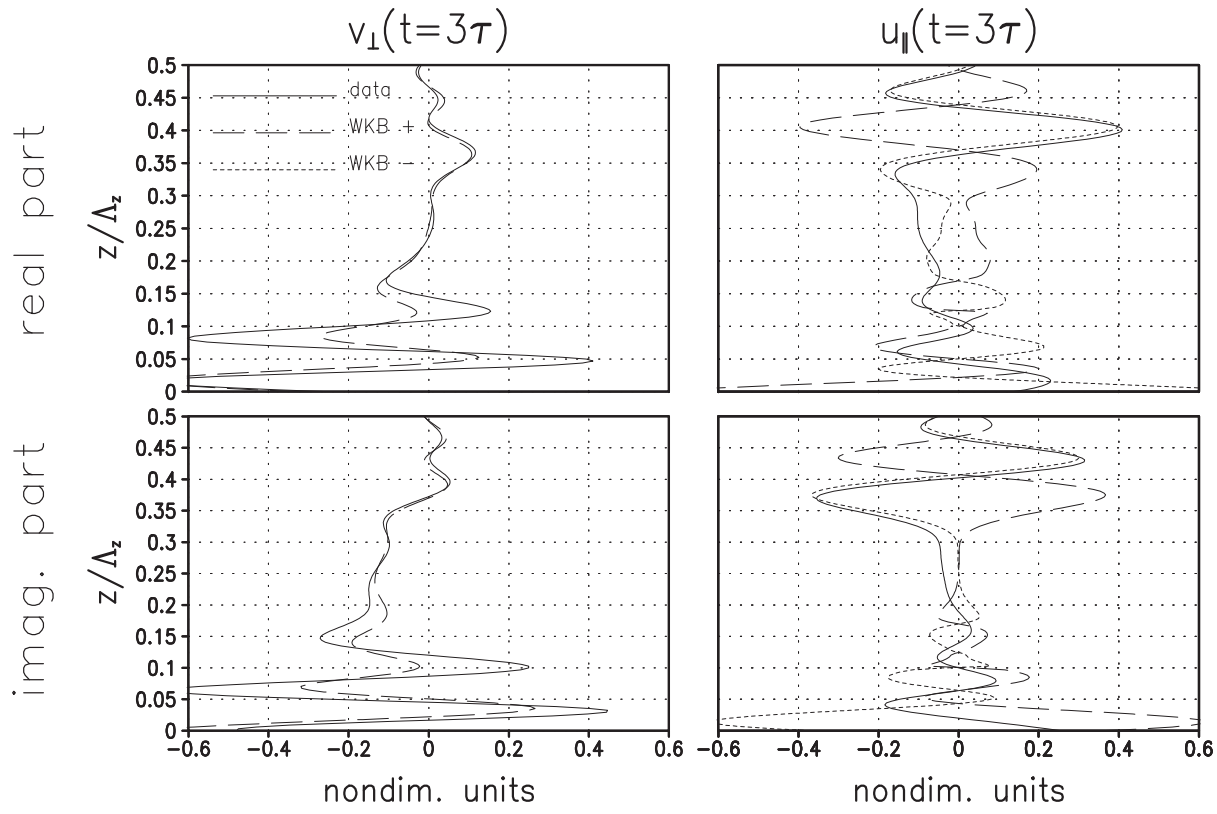

Figure 11: From the same integration as shown in Fig. 9 the real parts (top row) and imaginary parts (bottom) for $v_\perp$ (left column) and $u_\parallel$ (right) at $t = 3\tau = 30$ min, as well as the prediction of these fields from WKB theory using the two branches $\delta = \pm 1$.

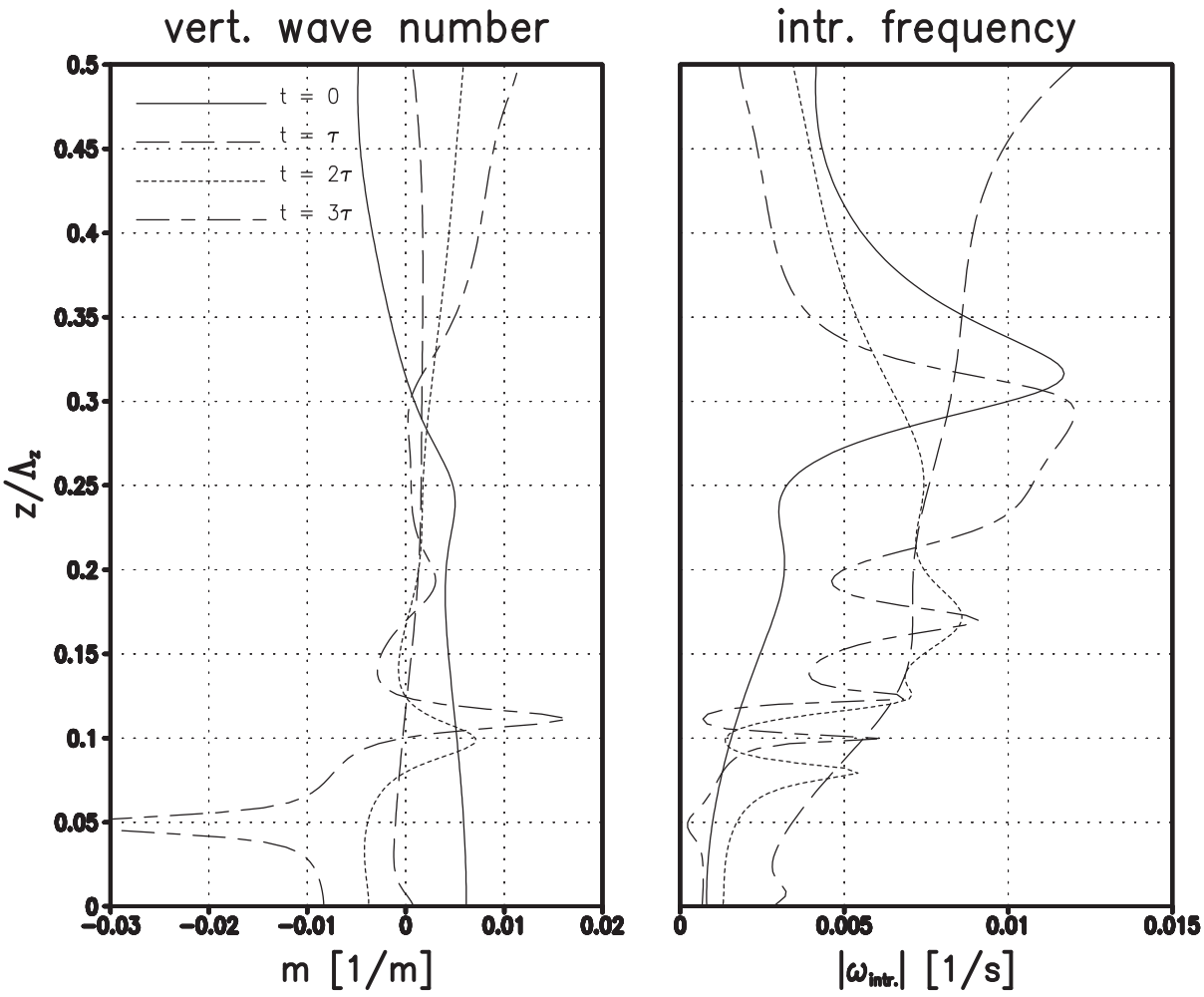

Figure 12: From the same integration as shown in Fig. 9 the vertical wavenumber (left panel) and the absolute value of the intrinsic frequency according to WKB theory (right) at four characteristic times.

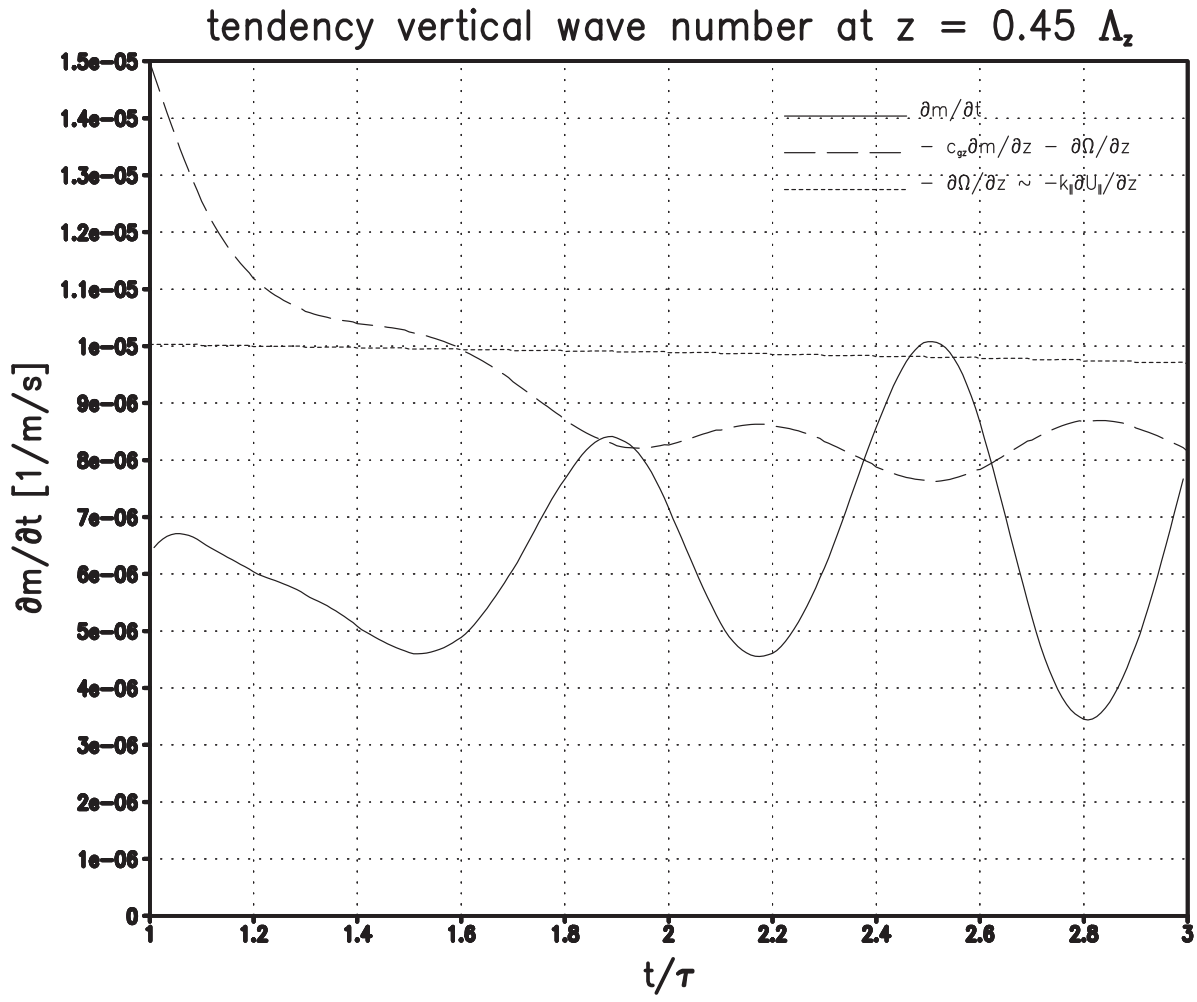

Figure 13: From the same integration as shown in Fig. 9 the tendency of vertical wavenumber at $z = 0.45\Lambda_z$, its prediction by WKB theory (long-dashed), and the part of the latter due to the transverse-wind gradient in the IGW $\partial U_\parallel/\partial z = \partial V_0/\partial z$ (short-dashed).

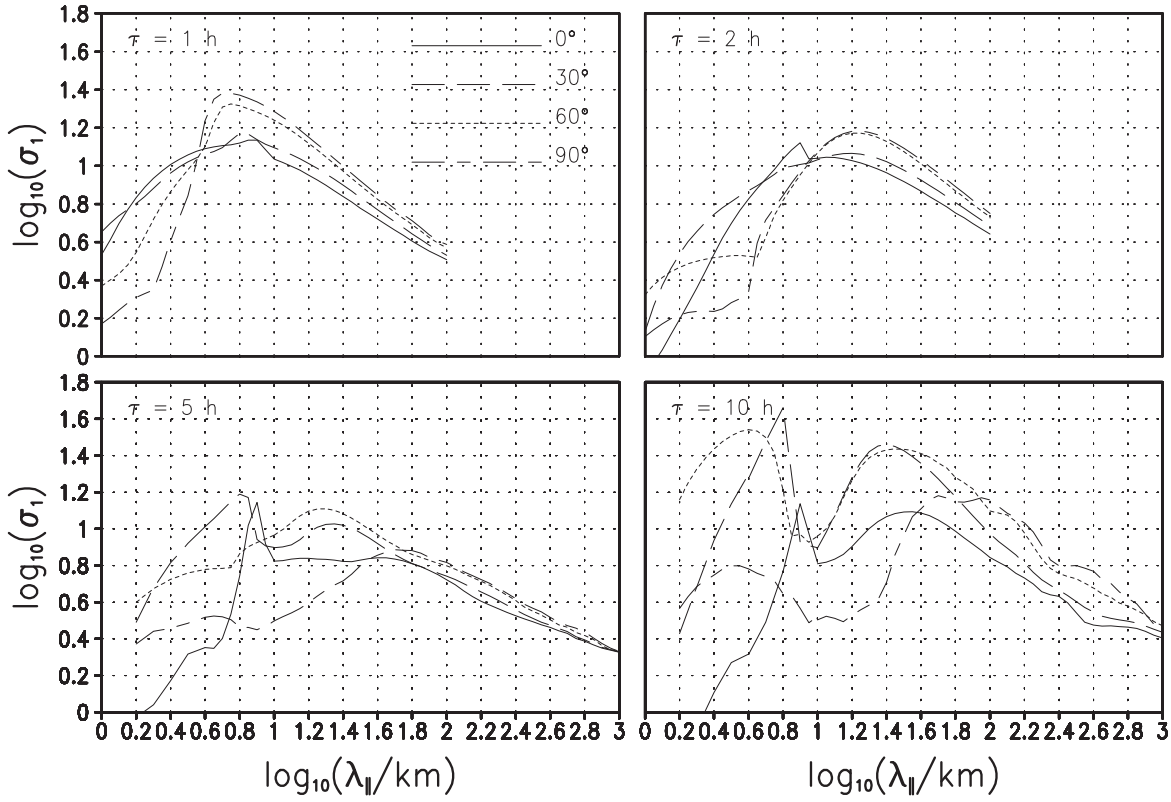

Figure 14: For the approximation of an IGW with $(a, \Lambda_z) = (0.9, 6\text{km})$ by a one-dimensional profile, the wavelength dependence of the growth factors of the strongest growing optimal perturbations at azimuth angle $\alpha = 0°, 30°, 60°$, and $90°$ for four different long optimization times τ.

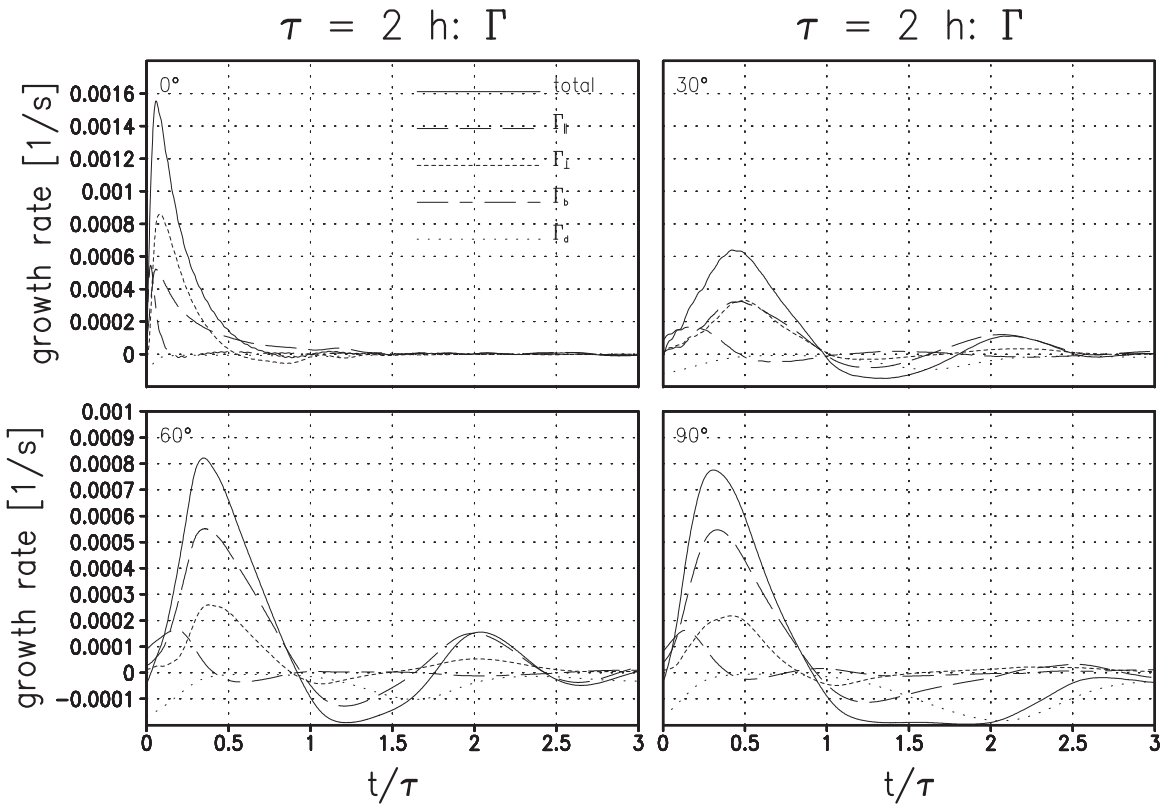

Figure 15: From an integration of the leading SVs (i.e. at most rapidly growing parallel wavelength), at azimuth angle $\alpha = 0°, 30°, 60°$, and $90°$ and optimization time $\tau = 2$ h, in an approximation of an IGW with $(a, \Lambda_z) = (0.9, 6\text{km})$ by a one-dimensional profile, the instantaneous growth rate and its decomposition.

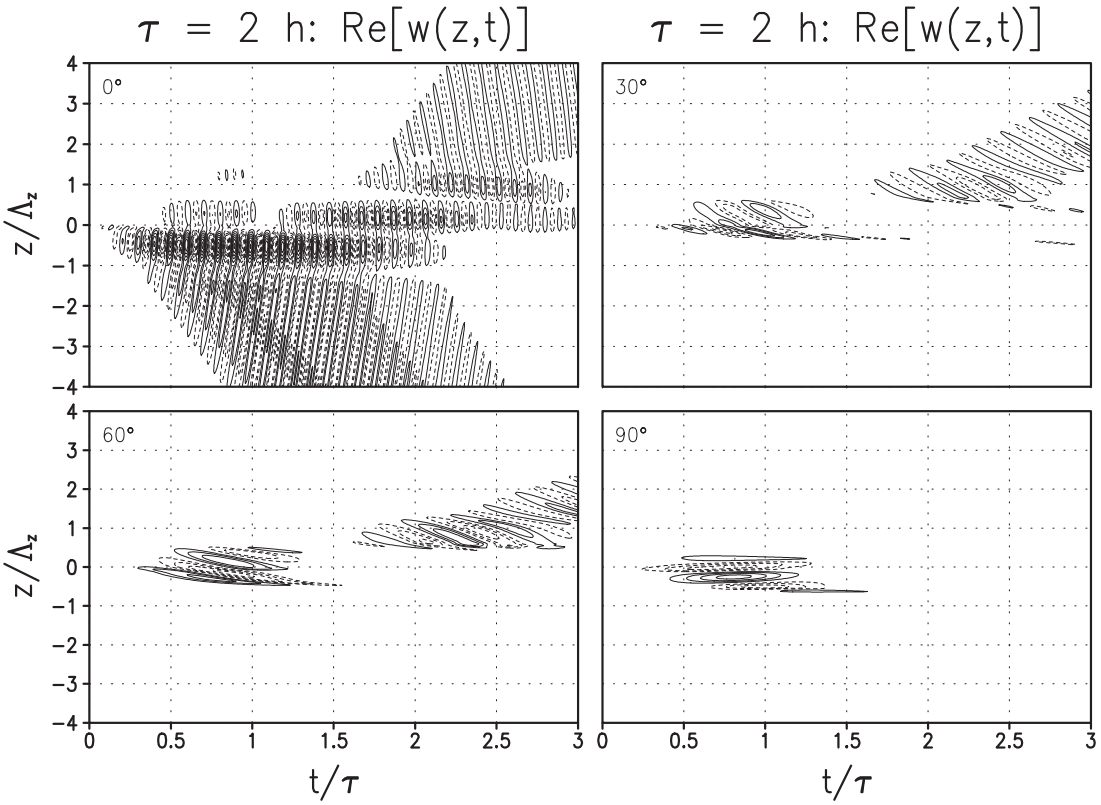

Figure 16: From the same integrations as shown in Fig. 15, the space-time dependent real part of the vertical wind in the perturbation. Contour intervals are in nondimensional units. Negative values are indicated by dashed contours. The zero contour is not shown.

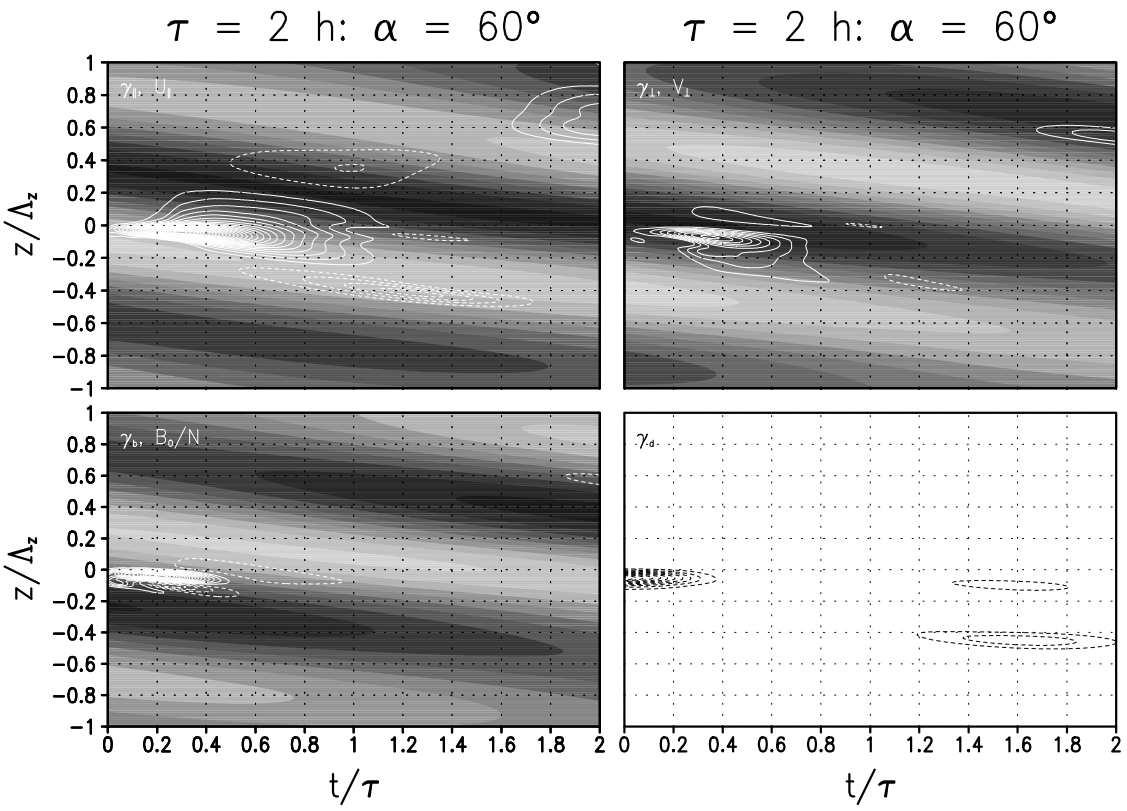

Figure 17: From the integration for $\alpha = 60°$ shown in Figs. 15 and 16, the space-time dependent IGW fields (shaded with shading interval 2 m/s), and the respective contributions to the instantaneous growth rate, as well as that of viscous-diffusive damping. For the growth-rate contributions the contour interval is $2 \cdot 10^{-4}\mathrm{s}^{-1}$. Negative values are indicated by dashed contours. The zero contour is not shown.

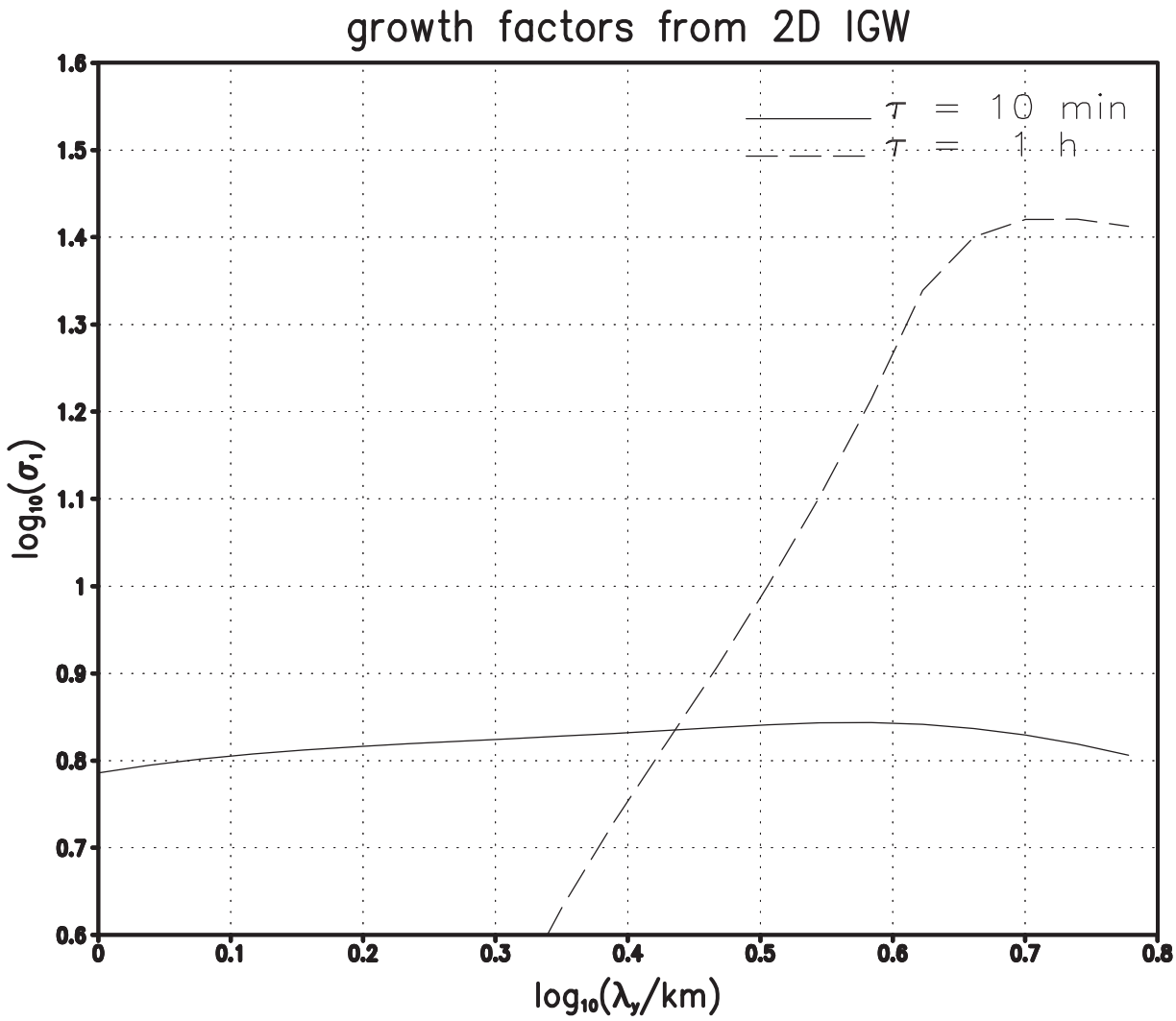

Figure 18: For the general IGW packet at $(a, \Lambda_z) = (0.9, 6\text{km})$ with complete time and space dependence, the growth factors of the leading SV for optimization times $\tau = 10$ min and 1 h, in their dependence of the wavelength λ_y in y-direction.

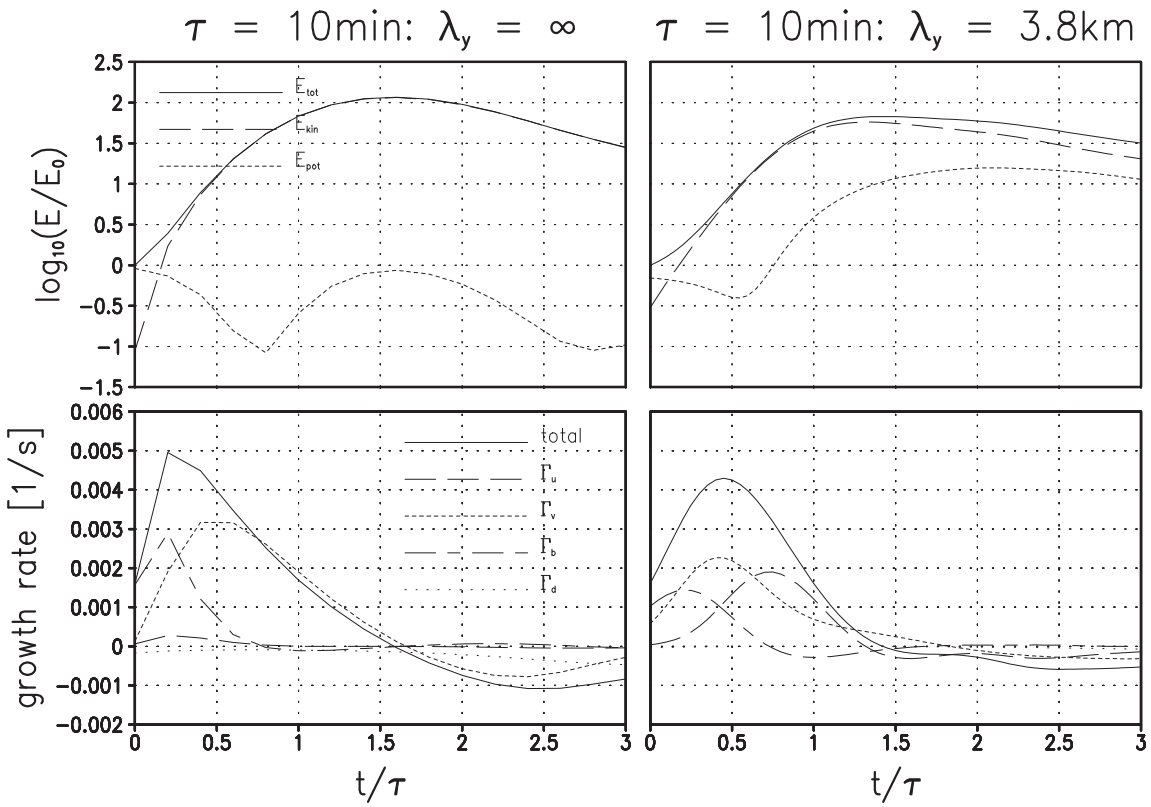

Figure 19: From integrations of the leading SV, for $\tau = 10$ min and at $\lambda_y = \infty$ (left column) or 3.8 km (right), of the general IGW packet at $(a, \Lambda_z) = (0.9, 6\text{km})$ with complete time and space dependence, the time dependence of kinetic, potential, and total energy (top row), and the corresponding instantaneous growth-rate decomposition (bottom).

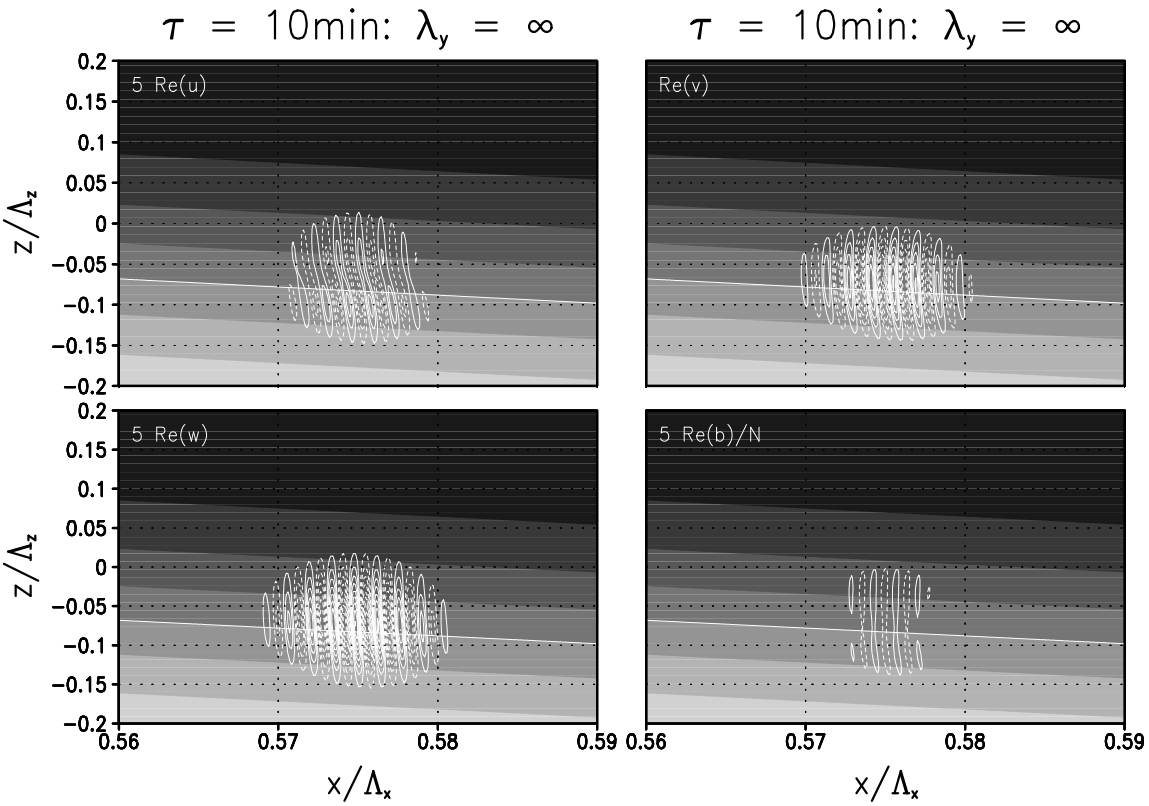

Figure 20: For the leading SV at $\tau = 10$ min and $\lambda_y = \infty$, of the general IGW packet at $(a, \Lambda_z) = (0.9, 6\text{km})$ with complete time and space dependence, the four dynamic fields at $t = \tau$ (identical isolines in arbitrary units for u, w and b/N, but five times contour interval for v, zero contour not drawn), together with the transverse-wind field V_0 of the IGW packet (shaded with interval 2 m/s, for better orientation the zero contour is indicated by a solid line), in the central region where the SV has significant amplitude.

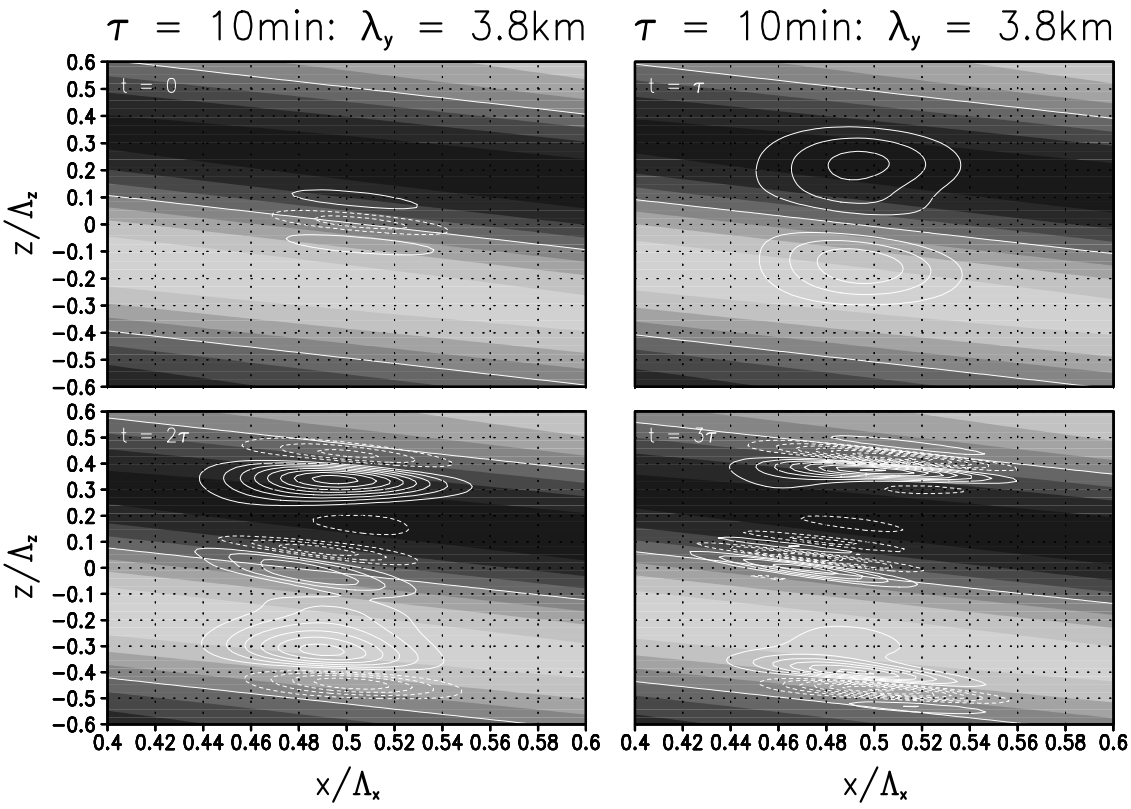

Figure 21: For the leading SV at $\tau = 10$ min and $\lambda_y = 3.8$ km, of the general IGW packet at $(a, \Lambda_z) = (0.9, 6\text{km})$ with complete time and space dependence, the buoyancy field at four characteristic time instances (identical isolines in arbitrary units, zero contour not drawn), together with the transverse-wind field V_0 of the IGW packet (shaded with interval 2 m/s, for better orientation the zero contour is indicated by a solid line), in the central region where the SV has significant amplitude.